Front. Phys.
https://doi.org/10.15302/frontphys.2026.125208
CN 11-5994/O4
ISSN 2095-0462

RESEARCH ARTICLE

Directional dynamics of the non-Hermitian skin effect

Bin Yi
Institute of Fundamental and Frontier Sciences, University of Electronic Science and Technology of China, Chengdu 610051, China

Received March 27, 2026; accepted June 9, 2026

ABSTRACT

The dynamical consequences of the non-Hermitian skin effect (NHSE), while increasingly studied, have so far received less systematic attention than its now well-characterized static properties. Here we contribute to this developing front by applying quantum Liang information flow (QLIF)—an inherently directional measure of causal influence—to the non-Hermitian Su-Schrieffer-Heeger model with non-reciprocal hopping. Unlike symmetric correlation functions, QLIF directly captures the directional asymmetry $\mathbb{T}_{R\to L} \neq \mathbb{T}_{L\to R}$ characteristic of non-reciprocal systems. We demonstrate a "scissors effect" where the asymmetry ΔT varies approximately linearly with the non-reciprocity parameter γ for small |γ|, and exhibits non-monotonic dependence on the skin length ξ, with optimal asymmetry at moderate skin localization. The velocity ordering v_{eff} (γ < 0) > v_{eff} (0) > v_{eff} (γ > 0) reveals NHSE-induced blocking of information flow against the skin direction. Three distinct temporal regimes emerge: light-cone-bounded spreading, γ-dependent stabilization, and coherent oscillations. These results establish the first quantitative connection between static skin localization and directional information dynamics, offering new insights into information propagation in non-reciprocal quantum systems.

Keywords quantum information, non-Hermitian system, quantum causal relation

Just Accepted

Directional Dynamics of the Non-Hermitian Skin Effect

Bin Yi

Institute of Fundamental and Frontier Sciences, University of Electronic Science and Technology of China, Chengdu 610051, China

Received March 27, 2026; accepted June 9, 2026

The dynamical consequences of the non-Hermitian skin effect (NHSE), while increasingly studied, have so far received less systematic attention than its now well-characterized static properties. Here we contribute to this developing front by applying quantum Liang information flow (QLIF)—an inherently directional measure of causal influence—to the non-Hermitian Su-Schrieffer-Heeger model with non-reciprocal hopping. Unlike symmetric correlation functions, QLIF directly captures the directional asymmetry $\mathbb{T}_{R\to L} \neq \mathbb{T}_{L\to R}$ characteristic of non-reciprocal systems. We demonstrate a "scissors effect" where the asymmetry $\Delta_{\mathbb{T}}$ varies approximately linearly with the non-reciprocity parameter γ for small $|\gamma|$, and exhibits non-monotonic dependence on the skin length ξ, with optimal asymmetry at moderate skin localization. The velocity ordering $v_{\text{eff}}(\gamma<0) > v_{\text{eff}}(0) > v_{\text{eff}}(\gamma>0)$ reveals NHSE-induced blocking of information flow against the skin direction. Three distinct temporal regimes emerge: light-cone-bounded spreading, γ-dependent stabilization, and coherent oscillations. These results establish the first quantitative connection between static skin localization and directional information dynamics, offering new insights into information propagation in non-reciprocal quantum systems.

Keywords quantum information, non-Hermitian system, quantum causal relation

I. INTRODUCTION

The non-Hermitian skin effect (NHSE)—the dramatic accumulation of all eigenstates at system boundaries under open boundary conditions—has emerged as a defining phenomenon in non-Hermitian physics [1–11]. Experimental realizations now span photonic lattices [12, 13], topolectrical circuits [14, 15], quantum walks [16, 17], and ultracold atoms [18]. While the relationship between non-reciprocal couplings and skin accumulation direction is well established in one-dimensional models [6, 10, 11] and has been extended to multilayer settings [19], recent works have shown that this correspondence can be nontrivially modified or even reversed in more general settings [20–22]. Much of this body of work has emphasized *static* properties—spectra, topological invariants, and eigenstate distributions [2, 23–30]—while *dynamical* aspects have only more recently received systematic attention [31–41]. A central open question is how the non-reciprocity parameter γ affects information propagation.

Traditional dynamical probes are inadequate for this task. Time-dependent correlation functions $\langle\sigma_i(t)\sigma_j(0)\rangle$ are inherently symmetric and cannot capture directional bias [7, 32]. The Lieb-Robinson bound [42, 43], which constrains information spreading in Hermitian systems, breaks down in the non-Hermitian case [44]—as demonstrated by supersonic modes observed on trapped-ion quantum computers [45]. The quasiparticle picture [46] also faces challenges with complex spectra and biorthogonal eigenstates [8, 47]. What is needed is a measure that directly quantifies *directional asymmetry* in information flow.

Quantum Liang information flow (QLIF) [48–50] provides precisely such a measure. QLIF quantifies the causal influence of one subsystem on another by comparing the entropy evolution with and without the coupling to a frozen subsystem [51, 52]. Unlike correlations, QLIF is inherently directional ($\mathbb{T}_{B\to A} \neq \mathbb{T}_{A\to B}$), making it ideally suited for non-reciprocal systems. Here we apply QLIF to the non-Hermitian SSH model [53] with non-reciprocal hopping $t_1 \pm \gamma$. We discover: (i) a "scissors effect" where $\Delta_{\mathbb{T}} = \mathbb{T}_{R\to L} - \mathbb{T}_{L\to R}$ varies linearly with γ for small γ; (ii) non-monotonic dependence on skin length ξ; (iii) velocity ordering $v_{\text{eff}}(\gamma<0) > v_{\text{eff}}(0) > v_{\text{eff}}(\gamma>0)$ revealing NHSE-induced blocking; and (iv) three distinct temporal regimes. These results establish the first quantitative link between skin localization and directional information dynamics.

II. MODEL

We consider a non-Hermitian Su-Schrieffer-Heeger (SSH) chain with N unit cells under open boundary conditions [6]:

$$H = \sum_{j=1}^{N} \mathbf{c}_j^\dagger \mathcal{T}_0\, \mathbf{c}_j + \sum_{j=1}^{N-1} \left(\mathbf{c}_{j+1}^\dagger \mathcal{T}_+\, \mathbf{c}_j + \text{H.c.} \right), \tag{1}$$

where $\mathbf{c}_j = (c_{\alpha,j}, c_{\beta,j})^T$ and

$$\mathcal{T}_0 = \begin{pmatrix} 0 & t_1+\gamma \\ t_1-\gamma & 0 \end{pmatrix}, \quad \mathcal{T}_+ = \begin{pmatrix} 0 & 0 \\ t_2 & 0 \end{pmatrix}. \tag{2}$$

Here t_1 (t_2) is the intracell (intercell) hopping, and γ parametrizes non-reciprocity [1]. The non-Hermitian SSH model is the canonical platform for studying the NHSE: Yao and Wang [6] established the modern theory of skin localization in this model, and it has since been realized experimentally in photonic lattices [12], topolectrical circuits [14, 15], and ultracold atoms [18]. Its bipartite structure additionally enables sublattice-resolved QLIF measurements that reveal measurement-geometry effects absent in single-band models (see Fig. 4).

For $\gamma \neq 0$, the non-Hermitian skin effect (NHSE) causes all eigenstates to localize exponentially at one boundary [6, 8]. The eigenstate envelope $|\psi_n| \sim r^n$ is governed by the skin parameter

$$r = \sqrt{\left|\frac{t_1-\gamma}{t_1+\gamma}\right|}, \tag{3}$$

and the associated skin length

$$\xi = \frac{1}{|\ln r|}, \tag{4}$$

which measures the localization length in units of lattice sites. $\gamma > 0$ ($r < 1$) gives left-boundary localization; $\gamma < 0$ ($r > 1$) gives right-boundary localization. In the Hermitian limit $\gamma \to 0$, $r \to 1$ and $\xi \to \infty$.

We set $t_1 = 1$, $t_2 = 0.5$, and $L = 42$ sites, scanning γ up to $|\gamma| = 0.4$ (the physically allowed range is $|\gamma| < t_1$). Details on the bulk spectrum and light-cone velocity are in the Supplemental Material [54].

III. QUANTUM LIANG INFORMATION FLOW

The quantum Liang information flow (QLIF) [48–50, 52] quantifies the causal influence of subsystem B on A through a freezing operation. Let $S_A(t) = -\mathrm{tr}[\rho_A \ln \rho_A]$ be the von Neumann entropy of A, and $H_{\not B}$ a modified Hamiltonian with all couplings to B removed. The instantaneous QLIF is defined as [48, 49]

$$T_{B\to A}(t) = \frac{\mathrm{d}S_A}{\mathrm{d}t} - \frac{\mathrm{d}S_{A\not B}}{\mathrm{d}t}, \tag{5}$$

where $S_{A\not B}$ is the entropy of A under frozen-B evolution (Fig. 1). Since both evolutions share the same initial state, $S_A(0) = S_{A\not B}(0)$, integrating Eq. (5) over time yields the equivalent cumulative form [48, 52]

$$\mathbb{T}_{B\to A}(t) = \int_0^t T_{B\to A}(t')\,\mathrm{d}t' = S_A(t) - S_{A\not B}(t), \tag{6}$$

which directly measures the total causal influence accumulated up to time t. We adopt this cumulative form throughout, as it avoids numerical differentiation and provides a more robust measure for finite-time dynamics. Unlike correlation functions, QLIF is inherently directional: $\mathbb{T}_{B\to A} \neq \mathbb{T}_{A\to B}$ in general.

Since the non-Hermitian time evolution $|\psi(t)\rangle = e^{-iHt}|\psi_0\rangle$ does not preserve the norm, we employ real-time normalization throughout:

$$\rho(t) = \frac{|\psi(t)\rangle\langle\psi(t)|}{\langle\psi(t)|\psi(t)\rangle}, \tag{7}$$

which ensures $\mathrm{tr}[\rho] = 1$ and positive semidefiniteness at all times. The reduced density matrix ρ_A and all entropy quantities are computed from this normalized state. We note that an alternative biorthogonal density matrix $\rho_{\mathrm{bi}} = |\psi_R\rangle\langle\psi_L|/\langle\psi_L|\psi_R\rangle$, constructed from both right- and left-evolving states, has been considered in the literature [55]. However, ρ_{bi} is not Hermitian in general and therefore the von Neumann entropy is not well-defined for it. Our choice of the right-state normalized density matrix in Eq. (7) is the standard framework for computing entanglement entropy in non-Hermitian systems [51].

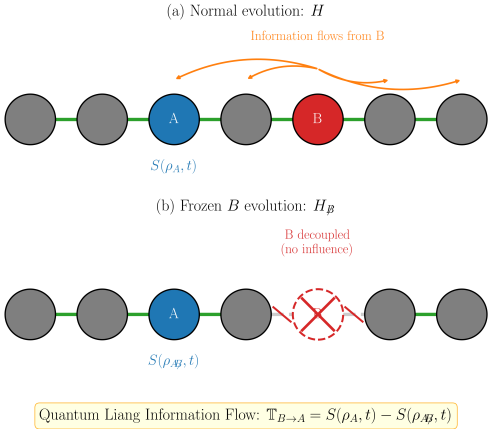

FIG. 1. Freezing operation for QLIF. (a) Normal evolution: all couplings active. (b) Frozen-B evolution: couplings to B removed. The QLIF is the entropy difference between (a) and (b).

The initial excitation is placed at the central unit cell $j_0 = \lceil N/2 \rceil$ ($N = L/2$), with observation sites A (left) and B (right) at equal distance d on opposite sides. For the scissors, sublattice, and skin-length analyses (Figs. 2–5), all three sites lie on the α sublattice ($\alpha\alpha\alpha$ configuration), ensuring $\Delta_{\mathbb{T}} = 0$ at $\gamma = 0$ by inversion symmetry. For the light-cone analysis (Fig. 6), the initial excitation is on the β sublattice; this does not affect the bulk dynamics, as confirmed in Fig. 4. Specific parameters are stated in each figure caption; implementation details are in the Supplemental Material [54].

IV. RESULTS

a. Scissors effect. In the Hermitian limit ($\gamma = 0$), spatial inversion symmetry ensures $\mathbb{T}_{R\to L}(t) = \mathbb{T}_{L\to R}(t)$; Fig. 2(a) confirms this with deviations below machine precision ($< 10^{-14}$). For $\gamma \neq 0$, this symmetry is broken: Fig. 2(b,c) displays the "scissors" pattern where the directional asymmetry $\Delta_{\mathbb{T}} = \mathbb{T}_{R\to L} - \mathbb{T}_{L\to R}$ is positive for $\gamma > 0$ (left-boundary skin localization enhances right-to-left flow) and negative for $\gamma < 0$. At intermediate times ($t \approx 10$), the cumulative QLIF can be either positive or negative, depending on the interplay between wavepacket spreading and interference effects.

To systematically characterize this dependence, we scan $|\gamma| \leq 0.4$ and extract $\Delta_{\mathbb{T}}$ at fixed times. Figure 3 reveals a key result: the sign rule

$$\mathrm{sgn}(\Delta_{\mathbb{T}}) = \mathrm{sgn}(\gamma) \tag{8}$$

holds throughout the entire range, directly addressing the open question of "how the behavior of NHSE is influenced by the variation of nonreciprocity" [40]. Crucially, the asymmetry exhibits *non-monotonic* γ-dependence: $|\Delta_{\mathbb{T}}|$ increases approximately linearly for small $|\gamma|$, peaks at moderate values ($|\gamma| \approx 0.15$–0.3), then decreases toward

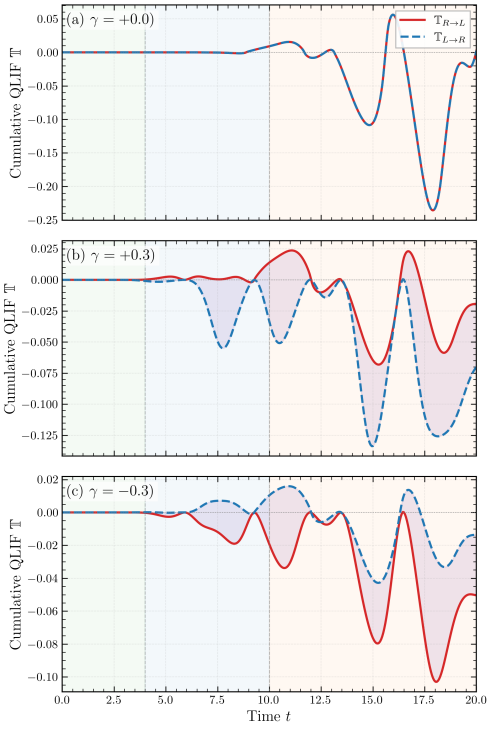

FIG. 2. Scissors effect in cumulative QLIF. Time evolution of $\mathbb{T}_{R\to L}$ (solid) and $\mathbb{T}_{L\to R}$ (dashed) for (a) $\gamma = 0$ (Hermitian, perfect overlap), (b) $\gamma = +0.3$, and (c) $\gamma = -0.3$. The shaded region highlights the directional asymmetry. Three temporal regimes are delineated by vertical dashed lines: (I) causal onset ($|\mathbb{T}| < \epsilon$, lasting until the light-cone arrival time $t_{\text{onset}} \approx d/v_{\text{eff}}$), (II) quasi-stationary growth (monotonic QLIF evolution with accumulating asymmetry), and (III) oscillatory regime (onset at the first local extremum of $\mathbb{T}$; period $T_{\text{osc}} \approx 2\pi/\Delta E$ set by intrinsic energy-level spacing). Initial state: $|\psi_0\rangle = |j_0, \alpha\rangle$ at the central unit cell; $\alpha\alpha\alpha$ configuration; $L = 42$, $d = 6$, $t_1 = 1$, $t_2 = 0.5$.

zero as $|\gamma| \to t_1$. The suppression at large $|\gamma|$ has a clear microscopic origin: the intracell hopping amplitudes are $t_1 + \gamma$ ($\alpha \to \beta$) and $t_1 - \gamma$ ($\beta \to \alpha$). As $\gamma \to t_1$, one direction becomes completely suppressed ($t_1 - \gamma \to 0$) while the other doubles ($t_1 + \gamma \to 2t_1$), making hopping perfectly unidirectional. The skin length $\xi \to 0$ [Eq. (4)] in this limit, so that the eigenstate amplitude ratio between the two observation sites, $r^{2d} = e^{-2d/\xi}$, diverges—one QLIF channel is exponentially suppressed relative to the other. However, because both channels vanish when the reverse hopping $t_1 - \gamma \to 0$ shuts down, their *difference* $\Delta_{\mathbb{T}}$ also vanishes. Paradoxically, the strongest NHSE produces the weakest measurable directional asymmetry—a key prediction for experiments seeking optimal operating regimes. The numerical convergence of $\Delta_{\mathbb{T}}$ with respect to time step, system size, and freezing-operation precision is documented in Appendix B 6, where the residual uncertainty on the displayed values is bounded by $\sim 2 \times 10^{-9}$.

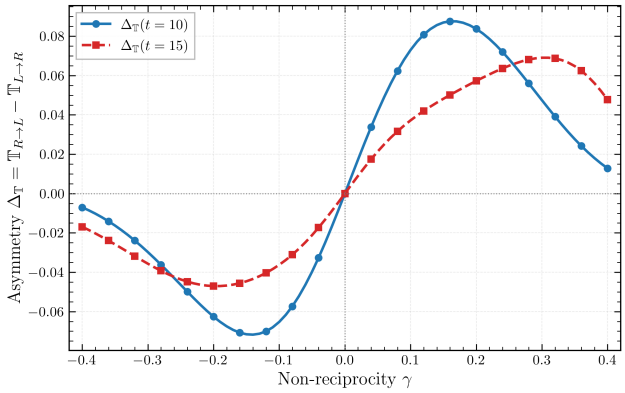

FIG. 3. Directional asymmetry $\Delta_{\mathbb{T}}$ versus γ at $t = 10$ (circles) and $t = 15$ (squares) for $|\gamma| \leq 0.4$. The sign rule $\text{sgn}(\Delta_{\mathbb{T}}) = \text{sgn}(\gamma)$ holds throughout. The non-monotonic behavior—peaking at moderate $|\gamma|$ and decreasing at larger $|\gamma|$—reflects competition between symmetry breaking and skin localization that confines dynamics to boundaries. Initial state: $|\psi_0\rangle = |j_0, \alpha\rangle$ at the central unit cell; $\alpha\alpha\alpha$ configuration; $L = 42$, $d = 6$, $t_1 = 1$, $t_2 = 0.5$.

b. Sublattice configuration. Figure 4 compares five sublattice configurations. Same-sublattice configurations ($\alpha\alpha\alpha$, $\beta\beta\beta$; solid lines) pass through the origin $(\gamma, \Delta_{\mathbb{T}}) = (0, 0)$ as required by inversion symmetry, and satisfy $\Delta_{\mathbb{T}}^{\beta\beta\beta}(\gamma) = \Delta_{\mathbb{T}}^{\alpha\alpha\alpha}(-\gamma)$, reflecting the sublattice exchange symmetry $\alpha \leftrightarrow \beta$ combined with $\gamma \to -\gamma$. Mixed-sublattice configurations (dashed lines) exhibit nonzero $\Delta_{\mathbb{T}}$ at $\gamma = 0$—a *structural* asymmetry arising from the inequivalent intracell and intercell hopping pathways. Despite these offsets, all curves show $d\Delta_{\mathbb{T}}/d\gamma > 0$ for small $|\gamma|$: a universal trend reflecting non-reciprocal hopping. All subsequent results use the $\alpha\alpha\alpha$ configuration to isolate the genuine NHSE signature.

c. Three temporal regimes. The time evolution exhibits three distinct regimes (Fig. 2): (I) At early times ($t \lesssim 4$), QLIF remains negligible until information propagates to observation sites; for $\gamma \neq 0$, the NHSE creates asymmetric onset times. (II) After the onset transient ($4 \lesssim t \lesssim 10$), QLIF enters a quasi-stationary regime where γ-dependent asymmetry is most clearly resolved. (III) At late times ($t \gtrsim 10$), persistent oscillations appear with period $T_{\text{osc}} \approx 2\pi/\Delta E$ determined by intrinsic energy-level spacing, independent of system size (see the Supplemental Material [54]). The NHSE protects oscillation amplitude because skin-localized eigenstates maintain high local probability density. All three regimes and their quantitative boundaries are L-independent for $L = 20$–80, confirming these as bulk properties [54].

d. Skin length dependence. While γ directly enters the Hamiltonian, the physically relevant quantity controlling eigenstate localization is the skin length ξ [Eq. (4)]. Recasting the γ-scan of Fig. 3 in terms of ξ (Fig. 5) identifies a characteristic scale: the QLIF asymmetry $|\Delta_{\mathbb{T}}|$ peaks at $\xi_{\text{opt}} \approx d$, comparable to the observation distance, delineating three regimes. In the *strong*

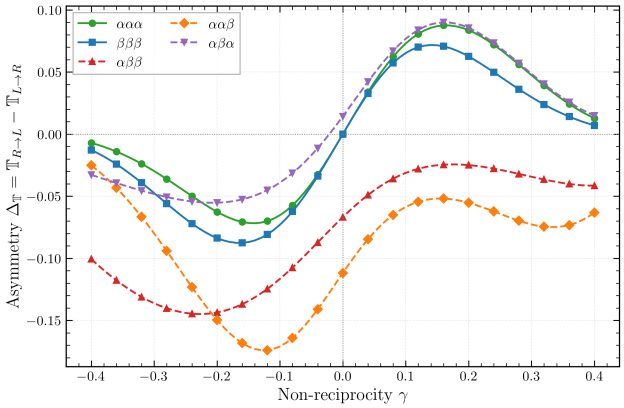

FIG. 4. Sublattice configuration effect on QLIF asymmetry. Solid lines: same-sublattice ($\alpha\alpha\alpha$, $\beta\beta\beta$) pass through the origin. Dashed lines: mixed-sublattice configurations show nonzero offset at $\gamma = 0$ due to structural asymmetry from bipartite hopping. Initial state: $|\psi_0\rangle = |j_0, \alpha\rangle$ at the central unit cell (for $\beta\beta\beta$: $|j_0, \beta\rangle$); $L = 42$, $t_1 = 1$, $t_2 = 0.5$, $t = 10$. Observation distance $d = 6$ for same-sublattice configurations; $d = 5$ for mixed configurations due to the sublattice offset.

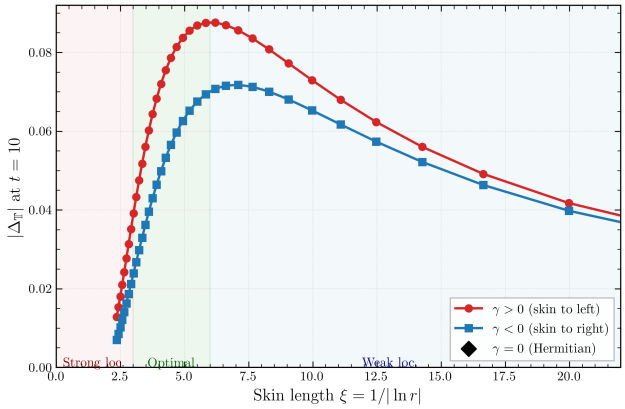

FIG. 5. QLIF asymmetry $|\Delta_{\mathbb{T}}|$ versus skin length ξ for $\gamma > 0$ (red circles) and $\gamma < 0$ (blue squares). The horizontal reference line at $|\Delta_{\mathbb{T}}| = 0$ marks the Hermitian limit ($\gamma = 0$, $\xi \to \infty$), where spatial inversion symmetry enforces $\Delta_{\mathbb{T}} = 0$; both branches converge to this limit as ξ increases. The nonmonotonic dependence reflects competition between symmetry breaking (favoring small ξ) and signal suppression (when eigenstates are too boundary-localized). Three regimes are shaded: strong localization (left), optimal asymmetry (center), and weak localization approaching the Hermitian limit (right). Initial state: $|\psi_0\rangle = |j_0, \alpha\rangle$ at the central unit cell; $\alpha\alpha\alpha$ configuration; $L = 42$, $d = 6$, $t_1 = 1$, $t_2 = 0.5$, $t = 10$.

localization regime ($\xi \ll d$), the controlling quantity is the relative probability ratio $r^{4d} = e^{-4d/\xi}$ between the two observation sites; the state becomes so directionally polarized that $|\Delta_{\mathbb{T}}|$ vanishes. In the *optimal regime* ($\xi \sim d$), symmetry breaking is strong while bulk transport remains viable, producing maximal asymmetry. In the *weak localization regime* ($\xi \gg d$), the system approaches the Hermitian limit. The $\gamma > 0$ and $\gamma < 0$ branches peak at different ξ values, reflecting the interplay between skin direction and measurement geometry; this branch asymmetry and the system-size independence of ξ_{opt} are confirmed in the Supplemental Material [54].

e. Mechanism summary. The behavior reported above can be traced through a chain linking the microscopic non-reciprocity γ to the QLIF asymmetry $\Delta_{\mathbb{T}}$. The first three steps are exact algebraic relations, verified to machine precision (cf. Appendix A 6): (1) nonreciprocal intracell hopping $t_1 \pm \gamma$ fixes the amplitude ratio r [Eq. (3)]; (2) r sets the skin length $\xi = 1/|\ln r|$ [Eq. (4)] and the eigenstate envelope $|\psi_n| \sim r^n$; (3) the similarity transformation translates this envelope into a propagator amplitude bias $r^{\pm d}$ between opposite directions [Eq. (9) below]. The final step (4) is dynamical: the bias enters the two opposite-direction QLIF channels asymmetrically, and the resulting $\Delta_{\mathbb{T}}$ is a *protocol response*—a functional of the freezing geometry, observation time and initial state on the same footing as the system parameters. This protocol-level character is what makes $\Delta_{\mathbb{T}}$ a dynamical witness of the NHSE, complementary to static localisation measures, and it underlies the qualitative features of Fig. 5 (the peak at $\xi \sim d$, the sign rule, and the multi-d behaviour).

f. NHSE blocking and velocity ordering. To probe the causal structure of information propagation, we measure the onset time t^*—the earliest time at which $|\mathbb{T}_{j_0 \to j_0 \pm d}| > \epsilon$ ($\epsilon = 10^{-6}$)—as a function of distance d for both rightward ($j_0 + d$) and leftward ($j_0 - d$) propagation. The frozen site is placed at the initial excitation j_0, so that QLIF directly measures causal influence from the source.

The light-cone structure is governed by the similarity transformation $H_{\text{NH}} = S^{-1} H_{\text{eff}} S$ (see the Supplemental Material [54]), which maps the non-Hermitian Hamiltonian to a Hermitian SSH chain with renormalized intracell hopping $\tilde{t}_1 = \sqrt{t_1^2 - \gamma^2}$ and unchanged t_2. This has two consequences. *First*, the wavefront speed $v_{\max}^{\text{GBZ}} = 2\min(\tilde{t}_1, t_2) = 2t_2 = 1.0$ is direction-independent and γ-independent for our parameters. *Second*, the signal amplitude is direction-dependent: the propagators satisfy

$$G_{\text{NH}}(j_0 \pm d,\, j_0;\, t) = r^{\pm d}\, G_{\text{eff}}(j_0 \pm d,\, j_0;\, t), \qquad (9)$$

where d is the unit-cell displacement and $r < 1$ for $\gamma > 0$. The non-Hermitian amplitudes in opposite directions therefore differ by a factor $r^{-2d} = e^{2d/\xi}$ (leftward amplified, rightward suppressed for $\gamma > 0$). The wavefront arrives simultaneously, but the skin-amplified direction crosses the detection threshold ϵ earlier, producing a larger apparent velocity.

This mechanism is confirmed by our two-directional analysis (Fig. 6): the velocity ordering reverses between directions,

$$v_{\text{eff}}^{\text{right}}(\gamma < 0) > v_{\text{eff}}^{\text{right}}(\gamma > 0), \quad v_{\text{eff}}^{\text{left}}(\gamma > 0) > v_{\text{eff}}^{\text{left}}(\gamma < 0), \qquad (10)$$

with $v_{\rm eff}^{\rm right}(\gamma) \approx v_{\rm eff}^{\rm left}(-\gamma)$ as required by the $\gamma \to -\gamma$ plus spatial inversion symmetry. At large distances ($d \gtrsim 10$), NHSE blocking becomes dramatic: propagation against the skin direction shows a sharp upturn as the exponential suppression r^d pushes the signal below the detection threshold. This provides a dynamical manifestation of the static eigenstate localization, demonstrating that the NHSE fundamentally alters not the speed but the *detectability* of information transport. A direct numerical verification of the propagator identity Eq. (9) and a side-by-side comparison of $\Delta_{\mathbb{T}}$ with the wavepacket center-of-mass drift $\Delta x(t)$ are provided in Appendix A 6: the two quantities share a common imaginary-gauge origin (same sign, same antisymmetry under $\gamma \to -\gamma$) but differ in shape, with the ξ-peak of $\Delta_{\mathbb{T}}$ being absent in the monotone $\Delta x(\xi)$.

V. DISCUSSION

A central experimental implication of our results is that moderate non-Hermiticity ($|\gamma| \approx 0.15$–0.3) maximizes the observable directional asymmetry, as confirmed by both the γ-scan (Fig. 3) and ξ-scan (Fig. 5). This provides concrete guidance for experimental realizations.

As a methodological advance, QLIF operates directly at the level of entropy production [51], bypassing the limitations of symmetric correlation functions and the breakdown of Lieb-Robinson bounds [42–44] in non-Hermitian systems. Our results extend recent Hermitian applications [52] to the non-Hermitian regime.

We note that our analysis relies on the standard correspondence between the non-reciprocity parameter γ and the skin accumulation direction in the one-dimensional SSH model [6]. However, in more general settings—such as higher-dimensional lattices, photon-mediated interactions, or waveguide-coupled arrays—the direction of eigenstate accumulation does not always follow that of the asymmetric couplings, and skin effect *reversal* can occur [20–22]. Investigating how QLIF signatures—particularly the sign rule Eq. (8) and the velocity ordering Eq. (10)—are modified in systems exhibiting such reversed NHSE constitutes an intriguing direction for future work.

We fix $t_2/t_1 = 0.5$ throughout, placing the system in the topological phase. While QLIF has been shown to capture Hermitian quantum phase transitions [52]—including both spectrum-wide localization transitions and ground-state critical points—the interplay between non-Hermitian topology and QLIF involves additional complexities such as the generalized Brillouin zone and non-Hermitian topological invariants [6, 28], which are beyond the scope of the present work. The systematic study of QLIF signatures across the non-Hermitian topological phase boundary ($t_2 = t_1$) will be addressed in a forthcoming publication. As a partial check that the phenomena reported here are not artifacts of the particular topological choice $t_2/t_1 = 0.5$, we repeat the scissors-effect analysis in the trivial phase ($t_2/t_1 = 1.5$) in Appendix D; the qualitative features—vanishing asymmetry in the Hermitian limit, the sign rule, and the approximate linearity of $\Delta_{\mathbb{T}}(\gamma)$ near $\gamma = 0$—are preserved across the phase boundary. More fundamentally, the directional QLIF signatures reported here do not rely on the SSH bipartite structure at all: we confirm in Appendix E that the scissors asymmetry, the sign rule $\mathrm{sgn}(\Delta_{\mathbb{T}}) = -\mathrm{sgn}(\text{skin direction})$, and the non-monotonic optimal-regime peak in $\Delta_{\mathbb{T}}(\gamma)$ are all reproduced on the Hatano–Nelson chain [7]—a single-band non-reciprocal model with no sublattice and no line-gap topology—establishing these features as intrinsic to non-Hermitian directionality rather than to SSH topology.

A directly implementable testbed is the class of photonic single-photon non-unitary quantum walks pioneered by Xiao *et al.* [17, 34], which already realise chiral-symmetric non-Hermitian topological dynamics with tunable gain–loss contrast. There, an internal two-level degree of freedom (the photon polarisation) plays the role of the model's two-band structure, polarisation-dependent loss provides the non-Hermitian knob, and walk steps furnish a discretised time axis. The site-resolved coincidence counts and chiral-basis wavefunction tomography demonstrated on this platform already supply, in principle, the single-particle reduced density matrix needed to evaluate the entropy $S(\rho_A)$ on a chosen subsystem. The QLIF protocol additionally requires a reference evolution in which the coupling to the chosen subsystem is removed at the freezing time; in a Floquet quantum walk this corresponds to inserting, at the relevant step, an operation that effectively decouples that subsystem from the rest of the network, after which the two entropy time-series are subtracted. Because the platform realises a Floquet rather than continuous-time model, the correspondence is qualitative and the predicted signatures should be regarded as universal consequences of the chirality of the NHSE rather than as quantitative parameter matches; in particular, the γ-sign scissors asymmetry (Fig. 3) and the skin-direction–dependent enhancement (Fig. 5) depend only on this chirality and should be accessible within the walk depths already demonstrated. Classical analogues in topolectrical circuits [15] and photonic mesh lattices [12] remain accessible as complementary platforms, though the von Neumann entropy underlying QLIF requires the genuinely single-particle setting that the photonic walk provides. Several directions also remain open theoretically: extensions to interacting systems [41] and higher-order skin effects [40].

VI. CONCLUSION

We have applied quantum Liang information flow to the non-Hermitian SSH model, establishing the first quantitative connection between skin localization and directional information dynamics. Our principal find-

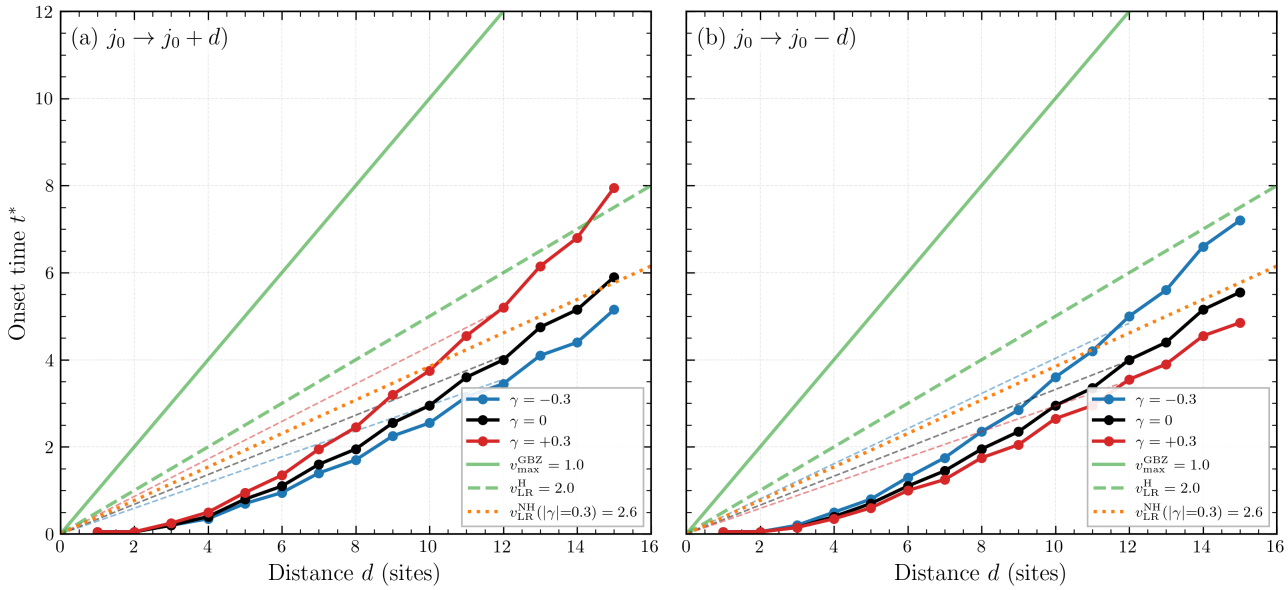

FIG. 6. Directional light-cone analysis. Onset time t^* (defined as the earliest time with $|\mathbb{T}| > \epsilon$, $\epsilon = 10^{-6}$) versus distance d ($d = 1$–15 sites) for rightward (left panel, $j_0 \to j_0 + d$) and leftward (right panel, $j_0 \to j_0 - d$) propagation at $\gamma = -0.3$ (blue), 0 (black), $+0.3$ (red). The velocity ordering reverses between directions, reflecting the $r^{\pm d}$ amplitude factor from Eq. (9). Solid green: $v_{\max}^{\mathrm{GBZ}} = 1.0$ (direction-independent GBZ group velocity); dashed green: Hermitian LR bound $v_{\mathrm{LR}}^{\mathrm{H}} = 2.0$; dotted orange: non-Hermitian LR estimate $v_{\mathrm{LR}}^{\mathrm{NH}}(|\gamma|{=}0.3) = 2.6$. Initial state: $|\psi_0\rangle = |j_0, \beta\rangle$ at the central unit cell; $L = 42$, $t_1 = 1$, $t_2 = 0.5$.

ings are: (i) a scissors effect with $\Delta_{\mathbb{T}} \propto \gamma$ for small $|\gamma|$; (ii) non-monotonic ξ-dependence with optimal asymmetry at moderate localization; (iii) velocity ordering $v_{\mathrm{eff}}(\gamma < 0) > v_{\mathrm{eff}}(0) > v_{\mathrm{eff}}(\gamma > 0)$ demonstrating NHSE blocking; and (iv) three distinct temporal regimes. These results establish QLIF as a powerful probe for non-Hermitian dynamics, opening new avenues for understanding directional information propagation in nonreciprocal quantum systems.

ACKNOWLEDGMENTS Y. B. acknowledges support from the National Natural Science Foundation of China (Grant No. 12404551) and the China Postdoctoral Science Foundation (Grant No. 2024M750339). The author thanks Sixun Huang and Xiangsan Liang for helpful discussions.

[1] E. J. Bergholtz, J. C. Budich, and F. K. Kunst, Exceptional topology of non-Hermitian systems, Rev. Mod. Phys. **93**, 015005 (2021).
[2] N. Okuma and M. Sato, Non-Hermitian topological phenomena: A review, Annu. Rev. Condens. Matter Phys. **14**, 83 (2023).
[3] Z. Gong, Y. Ashida, K. Kawabata, K. Takasan, S. Higashikawa, and M. Ueda, Topological phases of non-Hermitian systems, Phys. Rev. X **8**, 031079 (2018).
[4] Y. Ashida, Z. Gong, and M. Ueda, Non-Hermitian physics, Adv. Phys. **69**, 249 (2020).
[5] K. Kawabata, K. Shiozaki, M. Ueda, and M. Sato, Symmetry and topology in non-Hermitian physics, Phys. Rev. X **9**, 041015 (2019).
[6] S. Yao and Z. Wang, Edge states and topological invariants of non-Hermitian systems, Phys. Rev. Lett. **121**, 086803 (2018).
[7] N. Hatano and D. R. Nelson, Localization transitions in non-Hermitian quantum mechanics, Phys. Rev. Lett. **77**, 570 (1996).
[8] F. K. Kunst, E. Edvardsson, J. C. Budich, and E. J. Bergholtz, Biorthogonal bulk-boundary correspondence in non-Hermitian systems, Phys. Rev. Lett. **121**, 026808 (2018).
[9] T. E. Lee, Anomalous edge state in a non-Hermitian lattice, Phys. Rev. Lett. **116**, 133903 (2016).
[10] N. Okuma, K. Kawabata, K. Shiozaki, and M. Sato, Topological origin of non-Hermitian skin effects, Phys. Rev. Lett. **124**, 086801 (2020).
[11] K. Zhang, Z. Yang, and C. Fang, Correspondence between winding numbers and skin modes in non-Hermitian systems, Phys. Rev. Lett. **125**, 126402 (2020).
[12] S. Weidemann, M. Kremer, T. Helbig, T. Hofmann, A. Stegmaier, M. Greiter, R. Thomale, and A. Szameit, Topological funneling of light, Science **368**, 311 (2020).
[13] K. Wang, A. Dutt, C. C. Wojcik, and S. Fan, Topological complex-energy braiding of non-Hermitian bands, Nature **598**, 59 (2021).
[14] T. Helbig *et al.*, Generalized bulk-boundary correspondence in non-Hermitian topolectrical circuits, Nat. Phys. **16**, 747 (2020).
[15] T. Hofmann, T. Helbig, F. Schindler, N. Salgo, M. Brzezińska, M. Greiter, T. Kiessling, D. Wolf, A. Vollhardt, A. Kabaši, C. H. Lee, A. Bilić, R. Thomale, and T. Neupert, Reciprocal skin effect and its realization in a topolectrical circuit, Phys. Rev. Research **2**, 023265 (2020).
[16] T. Li, Y.-S. Zhang, and W. Yi, Two-dimensional quantum walk with non-Hermitian skin effects, Chin. Phys.

Lett. **38**, 030301 (2021).
[17] L. Xiao *et al.*, Non-Hermitian bulk-boundary correspondence in quantum dynamics, Nat. Phys. **16**, 761 (2020).
[18] E. Zhao, Z. Wang, C. He, S.-G. Peng, D. Yu, X. Liu, and G.-B. Jo, Two-dimensional non-Hermitian skin effect in an ultracold Fermi gas, Nature **637**, 565 (2025).
[19] J.-R. Li, C. Jiang, H. Su, D. Qi, L.-L. Zhang, and W.-J. Gong, Parity-dependent skin effects and topological properties in the multilayer nonreciprocal Su–Schrieffer–Heeger structures, Front. Phys. **19**, 33204 (2024).
[20] M. Yang and C. H. Lee, Reversing non-Hermitian skin accumulation with a non-local transverse switch, Commun. Phys. 10.48550/arXiv.2509.02686 (2025), accepted; arXiv:2509.02686.
[21] F. Roccati, M. Bello, Z. Gong, M. Ueda, F. Ciccarello, A. Chenu, and A. Carollo, Hermitian and non-Hermitian topology from photon-mediated interactions, Nat. Commun. **15**, 2400 (2024).
[22] J. Shi and A. N. Poddubny, Chiral dissociation of bound photon pairs for a non-Hermitian skin effect, Phys. Rev. Lett. **134**, 233602 (2025).
[23] X.-R. Wang, C.-X. Guo, Q. Du, and S.-P. Kou, State-dependent topological invariants and anomalous bulk-boundary correspondence in non-Hermitian topological systems with generalized inversion symmetry, Chin. Phys. Lett. **37**, 117303 (2020).
[24] R. Lin, T. Tai, L. Li, and C. H. Lee, Topological non-Hermitian skin effect, Front. Phys. **18**, 53605 (2023).
[25] C. H. Lee and R. Thomale, Anatomy of skin modes and topology in non-Hermitian systems, Phys. Rev. B **99**, 201103(R) (2019).
[26] L. Herviou, J. H. Bardarson, and N. Regnault, Defining a bulk-edge correspondence for non-Hermitian Hamiltonians via singular-value decomposition, Phys. Rev. A **99**, 052118 (2019).
[27] S. Longhi, Probing non-Hermitian skin effect and non-Bloch phase transitions, Phys. Rev. Research **1**, 023013 (2019).
[28] K. Yokomizo and S. Murakami, Non-Bloch band theory of non-Hermitian systems, Phys. Rev. Lett. **123**, 066404 (2019).
[29] A. Fan and S.-D. Liang, Complex energy plane and topological invariant in non-Hermitian systems, Front. Phys. **17**, 33501 (2022).
[30] X.-D. Xie, Z.-Y. Xue, and D.-B. Zhang, Variational quantum algorithms for scanning the complex spectrum of non-Hermitian systems, Front. Phys. **19**, 41202 (2024).
[31] Y.-A. Wang and L. Li, Non-Hermitian skin effects in fragmented Hilbert spaces of one-dimensional fermionic lattices, Chin. Phys. Lett. **42**, 037301 (2025).
[32] F. Song, S. Yao, and Z. Wang, Non-Hermitian skin effect and chiral damping in open quantum systems, Phys. Rev. Lett. **123**, 170401 (2019).
[33] W.-T. Xue, Y.-M. Hu, F. Song, and Z. Wang, Non-Hermitian edge burst, Phys. Rev. Lett. **128**, 120401 (2022).
[34] L. Xiao, W.-T. Xue, F. Song, Y.-M. Hu, W. Yi, Z. Wang, and P. Xue, Observation of non-Hermitian edge burst in quantum dynamics, Phys. Rev. Lett. **133**, 070801 (2024).
[35] Z. Li, L.-W. Wang, X. Wang, Z.-K. Wang, Y.-F. Lu, J.-J. Li, J. Hu, M.-H. Lu, and Y.-F. Chen, Observation of dynamic non-Hermitian skin effects, Nat. Commun. **15**, 6544 (2024).
[36] X. Li, J. Liu, and T. Liu, Localization–delocalization transitions in non-Hermitian Aharonov–Bohm cages, Front. Phys. **19**, 33211 (2024).
[37] T. Yoshida, S.-B. Zhang, T. Neupert, and N. Kawakami, Non-Hermitian mott skin effect, Phys. Rev. Lett. **133**, 076502 (2024).
[38] K. Shimomura and K. Kawabata, General criterion for non-Hermitian skin effects and application: Fock space skin effects in many-body systems, Phys. Rev. Lett. **133**, 136502 (2024).
[39] K. Zhang, C. Shu, and K. Sun, Algebraic non-Hermitian skin effect and generalized Fermi surface formula in arbitrary dimensions, Phys. Rev. X **15**, 10.1103/cwwd-bclc (2025), arXiv:2406.06682.
[40] Q.-B. Zeng, R. Lü, and L. You, Non-Hermitian skin effect edge, Phys. Rev. B **106**, 235411 (2022), arXiv:2203.08618.
[41] L. Li, C. H. Lee, S. Mu, and J. Gong, Critical non-Hermitian skin effect, Nat. Commun. **11**, 5491 (2020).
[42] E. H. Lieb and D. W. Robinson, The finite group velocity of quantum spin systems, Commun. Math. Phys. **28**, 251 (1972).
[43] S. Bravyi, M. B. Hastings, and F. Verstraete, Lieb-Robinson bounds and the generation of correlations and topological quantum order, Phys. Rev. Lett. **97**, 050401 (2006).
[44] B. Barch, Locality, correlations, information, and non-Hermitian quantum systems, Phys. Rev. B **110**, 094307 (2024).
[45] Y. Zhang, J. Carrasquilla, and Y. B. Kim, Observation of a non-Hermitian supersonic mode on a trapped-ion quantum computer, Nat. Commun. **16**, 3286 (2025).
[46] P. Calabrese and J. Cardy, Evolution of entanglement entropy in one-dimensional systems, J. Stat. Mech. **2005**, P04010 (2005).
[47] D. S. Borgnia, A. J. Kruchkov, and R.-J. Slager, Non-Hermitian boundary modes and topology, Phys. Rev. Lett. **124**, 056802 (2020).
[48] B. Yi and S. Bose, Quantum Liang information flow as causation quantifier, Phys. Rev. Lett. **129**, 020501 (2022).
[49] X. S. Liang, Information flow within stochastic dynamical systems, Phys. Rev. E **78**, 031113 (2008).
[50] X. S. Liang, Information flow and causality as rigorous notions ab initio, Phys. Rev. E **94**, 052201 (2016).
[51] L.-M. Chen, Y. Zhou, S. A. Chen, and P. Ye, Quantum entanglement and non-Hermiticity in free-fermion systems, Chin. Phys. Lett. **41**, 127302 (2024).
[52] R. Ghosh, B. Yi, and S. Bose, Quantum Liang information flow probe of causality across critical points, Phys. Rev. Lett. **134**, 150202 (2025).
[53] W. P. Su, J. R. Schrieffer, and A. J. Heeger, Solitons in polyacetylene, Phys. Rev. Lett. **42**, 1698 (1979).
[54] See Supplemental Material for model details, similarity transformation derivation, numerical methods, and scaling analysis.
[55] Y. Mao, P. Zhong, H. Lin, X. Wang, and S. Hu, Diagnosing thermalization dynamics of non-Hermitian quantum systems via GKSL master equations, Chin. Phys. Lett. **41**, 070301 (2024).

Supplemental Material: Directional Dynamics of the Non-Hermitian Skin Effect

Appendix A: Model Details and Light-Cone Velocity

1. Bulk Spectrum and Topological Phases

Under periodic boundary conditions, the Bloch Hamiltonian reads $\mathcal{H}(k) = \boldsymbol{d}(k) \cdot \boldsymbol{\sigma}$, where

$$d_x(k) = t_1 + t_2 \cos k, \quad d_y(k) = t_2 \sin k + i\gamma. \tag{A1}$$

For $\gamma = 0$, the dispersion is

$$E(k) = \sqrt{t_1^2 + t_2^2 + 2t_1 t_2 \cos k}, \tag{A2}$$

with gap $\Delta = 2|t_1 - t_2|$ and winding number $\nu = 1$ ($\nu = 0$) for $t_2 < t_1$ ($t_2 > t_1$) [1].

Table I summarizes NHSE parameters for representative γ values.

TABLE I. NHSE parameters for $t_1 = 1$, $L = 42$ sites.

γ	r	ξ	Direction	IPR
-0.4	1.53	2.4	Right	0.30
-0.2	1.22	4.9	Right	0.12
0	1.00	∞	—	0.024
$+0.2$	0.82	4.9	Left	0.12
$+0.4$	0.65	2.4	Left	0.30

2. Derivation of Light-Cone Velocity

Starting from the dispersion relation Eq. (A2), the quasiparticle group velocity is

$$v_g(k) = \frac{\partial E}{\partial k} = -\frac{t_1 t_2 \sin k}{E(k)}. \tag{A3}$$

To find the maximum of $|v_g(k)|$, we analyze

$$|v_g(k)| = \frac{t_1 t_2 |\sin k|}{\sqrt{t_1^2 + t_2^2 + 2t_1 t_2 \cos k}}. \tag{A4}$$

At the critical point $t_1 = t_2 \equiv t$, the dispersion simplifies to

$$E(k) = t\sqrt{2 + 2\cos k} = 2t \left|\cos \frac{k}{2}\right|, \tag{A5}$$

and the group velocity becomes

$$|v_g(k)| = \frac{t^2 \cdot 2|\sin(k/2)\cos(k/2)|}{2t|\cos(k/2)|} = t\left|\sin \frac{k}{2}\right|, \tag{A6}$$

which is maximized at $k = \pi$, yielding $v_{\max} = t$.

For general parameters, the maximum group velocity is given by

$$v_{\max} = \min(t_1, t_2). \tag{A7}$$

To prove this, assume $t_2 \le t_1$ and set $v_g(k^*) = t_2$. This gives $t_1 \sin k^* = E(k^*)$, which after squaring and simplifying yields $(t_1 \cos k^* + t_2)^2 = 0$, hence $\cos k^* = -t_2/t_1$. This solution exists when $t_2 \le t_1$, and the corresponding velocity is exactly $v_g(k^*) = t_2 = \min(t_1, t_2)$. This result is analogous to the transverse-field Ising model, where $v_{\max} = \min(J, h)$ with J the exchange coupling and h the transverse field [2].

Table II compares the exact numerical values with the approximate formula for $t_1 = 1$.

TABLE II. Comparison of exact maximum group velocity with the approximate formula $v_{\max} \approx \min(t_1, t_2)$ for $t_1 = 1$.

t_2	Phase	$v_{\max}$ (exact)	$\min(t_1, t_2)$
0.6	Topological	0.60	0.6
0.8	Topological	0.80	0.8
1.0	Critical	1.00	1.0
1.2	Trivial	1.00	1.0
1.4	Trivial	1.00	1.0

3. Similarity Transformation and GBZ Spectrum

The non-Hermitian SSH Hamiltonian H_{NH} can be mapped to an equivalent Hermitian model via a similarity transformation $H_{\mathrm{NH}} = S^{-1} H_{\mathrm{eff}} S$. Define the diagonal matrix S with

$$S_{\alpha,j} = r^{-j}, \quad S_{\beta,j} = r^{-j-1}, \tag{A8}$$

where j labels the unit cell and $r = \sqrt{(t_1 - \gamma)/(t_1 + \gamma)}$ [Eq. (3) in the main text]. Under this transformation:
Intracell hopping (j-independent):

$$\begin{aligned}(SH_{\mathrm{NH}}S^{-1})_{\alpha\beta} &= S_{\alpha,j}(t_1 + \gamma)S^{-1}_{\beta,j} = r^{-j}(t_1 + \gamma)r^{j+1} = (t_1 + \gamma)r,\\ (SH_{\mathrm{NH}}S^{-1})_{\beta\alpha} &= S_{\beta,j}(t_1 - \gamma)S^{-1}_{\alpha,j} = r^{-j-1}(t_1 - \gamma)r^{j} = (t_1 - \gamma)/r.\end{aligned} \tag{A9}$$

Setting $(t_1 + \gamma)r = (t_1 - \gamma)/r$ gives $r^2 = (t_1 - \gamma)/(t_1 + \gamma)$, confirming r as defined. The common value is

$$\tilde{t}_1 = (t_1 + \gamma)r = \sqrt{(t_1 + \gamma)(t_1 - \gamma)} = \sqrt{t_1^2 - \gamma^2}. \tag{A10}$$

Intercell hopping (cell $j \to j+1$):

$$(SH_{\rm NH}S^{-1})_{\alpha,j+1;\,\beta,j} = r^{-(j+1)} \cdot t_2 \cdot r^{j+1} = t_2,$$
$$(SH_{\rm NH}S^{-1})_{\beta,j;\,\alpha,j+1} = r^{-j-1} \cdot t_2 \cdot r^{j+1} = t_2. \quad \text{(A11)}$$

Thus $H_{\rm eff}$ is a Hermitian SSH model with intracell hopping $\tilde{t}_1 = \sqrt{t_1^2 - \gamma^2}$ and unchanged intercell hopping t_2. Equivalently, on the generalized Brillouin zone [3] with $e^{ik} \to re^{i\theta}$, the OBC spectrum is

$$E(\theta) = \pm\sqrt{\tilde{t}_1^2 + t_2^2 + 2\tilde{t}_1 t_2 \cos\theta}, \quad \text{(A12)}$$

and the maximum group velocity per unit cell is $\min(\tilde{t}_1, t_2)$, giving

$$v_{\max}^{\rm GBZ}(\gamma) = 2\min\big(\sqrt{t_1^2 - \gamma^2},\ t_2\big) \quad \text{(A13)}$$

in units of sites per time. This velocity is *direction-independent*: the GBZ dispersion Eq. (A12) is symmetric in $\theta \to -\theta$, so the wavefront propagates at the same speed in both directions.

4. Lieb-Robinson Bound and Its Breakdown

For Hermitian systems, the Lieb-Robinson theorem [4, 5] provides a rigorous upper bound on information propagation:

$$\|[A_x(t), B_0]\| \le C\|A\|\|B\|e^{-a(|x| - v_{\rm LR}|t|)}, \quad \text{(A14)}$$

where $v_{\rm LR} \sim 2J_{\max}$. For the Hermitian SSH model ($\gamma = 0$): $v_{\rm LR}^{\rm H} = 2\max(t_1, t_2) = 2.0$.

In non-Hermitian systems, LR bounds generically break down [6–8]. The non-unitary evolution operator e^{-iHt} can amplify signals along certain directions, enabling correlations to spread faster than the Hermitian limit. A naive upper bound using the maximum hopping amplitude $J_{\max} = \max(t_1 + |\gamma|, t_2)$ gives $v_{\rm LR}^{\rm NH} = 2J_{\max}$, which is looser than the Hermitian bound.

5. Direction-Dependent Onset Times

Using the propagator relation Eq. (9) in the main text, the direction-dependent effective velocities are listed in Table III. The symmetry $v_{\rm eff}^{\rm right}(\gamma) \approx v_{\rm eff}^{\rm left}(-\gamma)$ reflects the $\gamma \to -\gamma$ plus spatial inversion equivalence.

That all effective velocities exceed $v_{\rm LR}^{\rm H} = 2.0$ is consistent with the generic LR bound breakdown in non-Hermitian systems [6–8].

6. Numerical Verification of the Imaginary-Gauge Propagator Identity and Comparison with Wavepacket Drift

This appendix provides direct numerical evidence for the propagator identity Eq. (9) of the main text and a side-by-side comparison of the QLIF asymmetry $\Delta_{\mathbb{T}}$ with the wavepacket center-of-mass drift $\Delta x(t) = \langle x(t)\rangle - j_0$, the latter serving as a conventional non-Hermitian transport diagnostic. All data are obtained for $L = 42$, $t_1 = 1$, $t_2 = 0.5$, observation time $t_{\rm obs} = 10$, with a single-site initial state $|\psi_0\rangle = |j_0\rangle$ at the central α-site $j_0 = 20$, and observation sites placed at $j_0 \mp 2d_{\rm cells}$ ($\alpha\alpha\alpha$ configuration). Figure 1 summarizes the four diagnostics.

TABLE III. Direction-dependent effective velocities for $t_1 = 1$, $t_2 = 0.5$, $L = 42$, extracted from linear fits to $t^*(d)$ for $d \le 10$.

γ	$v_{\rm eff}^{\rm right}$	$v_{\rm eff}^{\rm left}$	ratio
-0.3	3.38	2.48	1.36
0	2.93	3.01	0.97
$+0.3$	2.32	3.40	0.68

a. Panel (a): exact match between data and the similarity transformation. For $\gamma = 0.1, 0.2, 0.3$ and all distances d = 1–9 sites, the measured propagator ratios agree with the staircase prediction $(S_{i,i}/S_{j,j})^2$ from $S_{\alpha,n} = r^{-n}$, $S_{\beta,n} = r^{-n-1}$ [Eq. (96) of this Supplemental Material] to better than 10^{-4}, spanning two decades of the bias ratio. The exact left-right product $|G_{\rm NH}(j_0{+}d)/G_{\rm eff}|^2 \cdot |G_{\rm NH}(j_0{-}d)/G_{\rm eff}|^2 = 1$ at all d confirms the diagonal structure of S. The bias is therefore not a smooth $r^{|d|}$ in site distance but a unit-cell staircase: each step of two sites multiplies the squared ratio by r^2. This is the imaginary-gauge content of the directional NHSE that the QLIF asymmetry inherits.

b. Panel (b): $\Delta_{\mathbb{T}}(\gamma)$ at multiple d. The QLIF asymmetry is antisymmetric under $\gamma \to -\gamma$ at machine precision, consistent with the sign rule Eq. (8). It exhibits a peak at $\xi \sim d_{\rm site}$ (e.g., $d = 3$: peak at $\gamma \approx 0.15$, $\xi \approx 6.6$; $d = 4$: peak at $\gamma \approx 0.20$, $\xi \approx 4.9$), then decays toward zero at both $|\gamma|$ extremes. Peak amplitudes drop by more than an order of magnitude from $d = 3$ to $d = 4$, faster than the r^{2d} bias alone: the Hermitian baseline $|G_{\rm eff}(2d, t)|^2$ that multiplies the bias also depends on d through the SSH light-cone structure, contributing an additional d-dependent suppression.

c. Panels (c)–(d): comparison with wavepacket drift. The wavepacket drift $\Delta x(\gamma)$ is monotone in γ, takes the same sign as the dominant skin direction (negative for $\gamma > 0$, leftward), and is independent of the QLIF observation distance d. The Hermitian-limit residual $\Delta x(\gamma = 0) \approx +0.55$ originates from the sublattice asymmetry of the α-site initial state and is unrelated to nonreciprocity. Panel (d) plots $\Delta_{\mathbb{T}}$ and Δx on a common ξ axis for $d = 4$, $\gamma > 0$: both quantities point leftward (same sign) and share a common imaginary-gauge origin via the $r^{\pm d}$ bias, but their shapes are qualitatively different—$\Delta x(\xi)$ is monotone (saturating in the strong-skin limit $\xi \to 0$), while $\Delta_{\mathbb{T}}(\xi)$ exhibits a pronounced peak at $\xi \sim d_{\rm site}$ before being suppressed. The peak

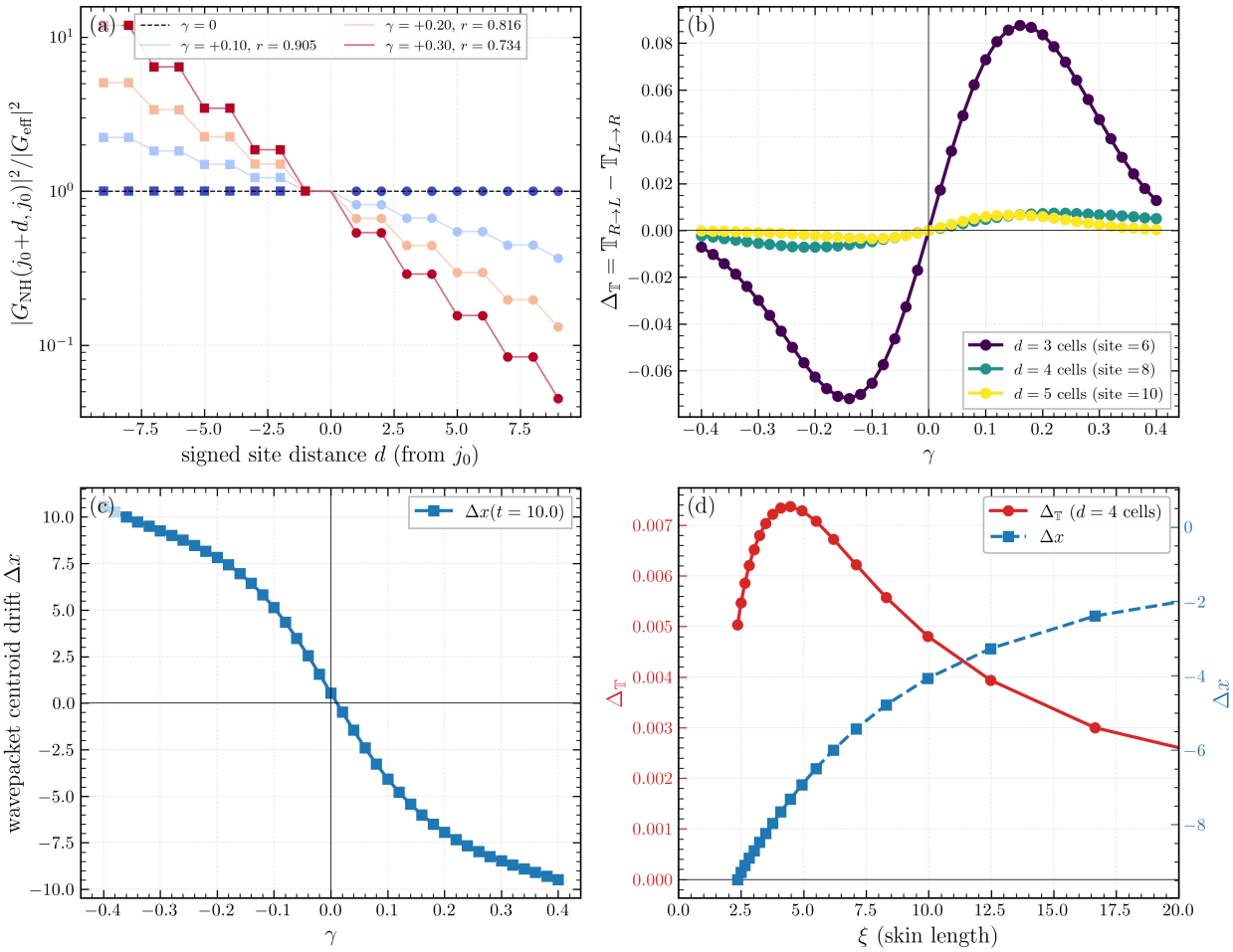

FIG. 1. Numerical verification of the imaginary-gauge picture and benchmarking against a conventional transport diagnostic. (a) Propagator amplitude ratio $|G_{\rm NH}(j_0 \pm d, j_0; t)|^2/|G_{\rm eff}(j_0 \pm d, j_0; t)|^2$ versus signed site distance, on a logarithmic scale, for $\gamma = 0, +0.1, +0.2, +0.3$ (circles: right-going; squares: left-going; staircases: similarity-transform prediction $(S_{i,i}/S_{j,j})^2$). (b) QLIF asymmetry $\Delta_{\mathbb{T}}(\gamma)$ for unit-cell observation distance $d = 3, 4, 5$. (c) Wavepacket center-of-mass drift $\Delta x(\gamma)$ at $t_{\rm obs} = 10$. (d) $\Delta_{\mathbb{T}}$ (red, left axis) and Δx (blue, right axis) versus the skin length ξ on the $\gamma > 0$ branch.

structure is a specific signature of the entropy-difference construction of QLIF: in the strong-skin limit the normalization $|\psi(t)|^2$ becomes concentrated at the boundary, suppressing bulk-site occupation and therefore the local conditional entropies that QLIF integrates. This feature is absent in Δx and identifies QLIF as a complementary, rather than redundant, diagnostic of non-Hermitian directional dynamics.

Appendix B: Numerical Methods

1. Exact Diagonalization

We numerically diagonalize the non-Hermitian SSH Hamiltonian using standard linear algebra routines. For non-Hermitian matrices, we compute both right and left eigenvectors, though for QLIF calculations only the right eigenvectors are needed.

2. Time Evolution and QLIF Implementation

For a single-particle state $|\psi\rangle = \sum_j \psi_j c_j^\dagger |0\rangle$, the site entropy reduces to binary entropy:

$$S_A = -|\psi_A|^2 \ln |\psi_A|^2 - (1 - |\psi_A|^2) \ln(1 - |\psi_A|^2). \quad \text{(B1)}$$

The freezing operation sets all matrix elements connected to site B to zero:

$$(H_{\not B})_{ij} = \begin{cases} 0 & \text{if } i = B \text{ or } j = B, \\ H_{ij} & \text{otherwise.} \end{cases} \quad \text{(B2)}$$

Time evolution is performed via exact diagonalization:

$$|\psi(t)\rangle = e^{-iHt}|\psi_0\rangle = \sum_n e^{-iE_n t}|n\rangle\langle n|\psi_0\rangle, \quad \text{(B3)}$$

where $\{E_n, |n\rangle\}$ are eigenvalues and right eigenvectors. For non-Hermitian H, biorthogonal normalization is employed.

3. Inverse Participation Ratio (IPR)

The inverse participation ratio (IPR) is a standard measure of localization [9] and has been widely used to characterize the skin effect in non-Hermitian systems [10, 11]. It is defined as

$$\mathrm{IPR} = \sum_j |\psi_j|^4 \Big/ \left(\sum_j |\psi_j|^2 \right)^2, \tag{B4}$$

ranging from $1/L$ (extended) to 1 (fully localized).

Here we derive the IPR for eigenstates exhibiting the non-Hermitian skin effect.

For a skin-effect eigenstate localized at the left boundary, the probability amplitude decays exponentially:

$$|\psi_n|^2 = A\, r^{2(n-1)}, \quad n = 1, 2, \ldots, N, \tag{B5}$$

where n labels the unit cell, r is the skin parameter [Eq. (3) in the main text], and A is the normalization constant.

a. Normalization. From $\sum_{n=1}^{N} |\psi_n|^2 = 1$:

$$A \sum_{n=1}^{N} r^{2(n-1)} = A \frac{1 - r^{2N}}{1 - r^2} = 1, \tag{B6}$$

giving

$$A = \frac{1 - r^2}{1 - r^{2N}}. \tag{B7}$$

b. IPR calculation. The IPR is

$$\begin{aligned} \mathrm{IPR} &= \sum_{n=1}^{N} |\psi_n|^4 = A^2 \sum_{n=1}^{N} r^{4(n-1)} \\ &= A^2 \frac{1 - r^{4N}}{1 - r^4} = \left(\frac{1 - r^2}{1 - r^{2N}} \right)^2 \frac{1 - r^{4N}}{(1 - r^2)(1 + r^2)} \\ &= \frac{(1 - r^2)(1 - r^{4N})}{(1 - r^{2N})^2 (1 + r^2)}. \end{aligned} \tag{B8}$$

Using the identity $1 - r^{4N} = (1 - r^{2N})(1 + r^{2N})$:

$$\mathrm{IPR}_{\mathrm{th}} = \frac{1 - r^2}{1 + r^2} \cdot \frac{1 + r^{2N}}{1 - r^{2N}}. \tag{B9}$$

c. Limiting cases.

- **Strong localization** ($r \ll 1$, N large): IPR $\to (1 - r^2)/(1 + r^2) \to 1$.
- **Extended states** ($r = 1$): Using L'Hôpital's rule, IPR $\to 1/N$, the expected value for uniform distribution.
- **Finite-size correction**: For $r < 1$ and large N, IPR $\approx (1 - r^2)/(1 + r^2)$.

The IPR values listed in Table I are obtained from direct numerical diagonalization, which includes finite-size corrections and deviations from the idealized exponential decay near boundaries. For the Hermitian case ($r = 1$), the table correctly shows IPR $= 1/L \approx 0.024$ for $L = 42$ sites.

4. Oscillation Analysis

Late-time QLIF oscillations have period $T_{\mathrm{osc}} \approx 2.2$ independent of system size L, ruling out finite-size boundary reflections. The period is determined by intrinsic energy-level spacing: $T_{\mathrm{osc}} \sim 2\pi/\Delta E$ where $\Delta E \approx 2.9$ matches the bulk bandwidth.

The NHSE protects oscillation amplitude: comparing $L = 20$ to $L = 120$, the Hermitian amplitude decays by $\sim 3\times$ while the non-Hermitian ($\gamma = 0.3$) amplitude decays by only $\sim 1.3\times$, because skin-localized eigenstates maintain high local probability density.

5. Sublattice Configuration for QLIF Measurements

As discussed in the main text (Fig. 4), mixed-sublattice configurations introduce a structural asymmetry $|\Delta_{\mathbb{T}}| \sim 0.07$ at $t = 10$ even for $\gamma = 0$, while same-sublattice configurations ($\alpha\alpha\alpha$, $\beta\beta\beta$) preserve inversion symmetry to machine precision ($\sim 10^{-15}$). To isolate genuine non-Hermitian effects, the observation distance d is chosen as an even integer to maintain the same sublattice, with $d = 6$ (3 unit cells) as the standard configuration.

6. Numerical Convergence and Error Analysis

The QLIF evaluation involves two potential sources of numerical error: (i) finite system size L, and (ii) the practical implementation of site freezing. The time step dt does not contribute, because the propagator e^{-iHt} is constructed via exact matrix exponentiation (`scipy.linalg.expm`) rather than an iterative integrator: across $dt \in \{0.005, 0.01, 0.02, 0.05, 0.1\}$ the value $\Delta_{\mathbb{T}}(t{=}10) = 4.7479844544 \times 10^{-2}$ is reproduced bit-for-bit, so dt enters only through the spacing of the cumulative-QLIF curve and carries no truncation error. We quantify the two remaining contributions at the working point $t_1 = 1$, $t_2 = 0.5$, $\gamma = 0.3$, $d = 6$, $t = 10$; the results are summarized in Fig. 2.

a. System size. For $L \in \{20, 30, 42, 60, 80\}$ with $d = 6$ held fixed in lattice-site units, $\Delta_{\mathbb{T}}$ stabilizes beyond $L \approx 30$: the value at $L = 42$ agrees with $L = 80$ to better than 2×10^{-9} [Fig. 2(a)]. The small $L = 20$ deviation reflects edge proximity of the observation sites and is already removed at $L = 30$, well below our working $L = 42$. At $L = 60$ the residual approaches the floating-point cancellation floor $|\Delta_{\mathbb{T}}|\, \epsilon \approx 10^{-17}$ set by subtracting two near-identical $\mathcal{O}(10^{-2})$ values in double precision; the underlying physical correction may be smaller still but is no longer resolvable.

b. Freezing operation. We compare the hard-freezing scheme used in the main text (zeroing out the row and column of the frozen site) with a soft-freezing scheme that adds a large on-site chemical potential $\mu\, |\mathrm{site}\rangle\langle\mathrm{site}|$ to H. The two schemes coincide in

the limit $\mu \to \infty$. Across $\mu \in \{10, 10^2, \ldots, 10^8\}$ the soft-freeze value converges to the hard-freeze value as $1/\mu^2$ [Fig. 2(b)], reaching agreement to 1.45×10^{-9} at $\mu = 10^4$ and saturating at floating-point precision for $\mu \geq 10^6$. The hard-freezing scheme is therefore the exact $\mu \to \infty$ limit of soft freezing, and the systematic error of this implementation is negligible.

c. Hermitian baseline. An independent consistency check is the $\gamma = 0$ limit, where time-reversal symmetry enforces $\mathbb{T}_{R\to L}(t) = \mathbb{T}_{L\to R}(t)$ identically. This is verified on the Hatano–Nelson chain in Appendix E: the residual asymmetry is bounded by $\sim 10^{-15}$ across the entire evolution window, confirming that any asymmetry reported in the main text is unambiguously attributable to $\gamma \neq 0$ rather than to numerical artifacts.

d. Error estimate for main-text figures. Combining the time-step and system-size residuals in quadrature, $\sigma_{\Delta_\mathbb{T}} = \sqrt{\sigma_{dt}^2 + \sigma_L^2} \approx 2 \times 10^{-9}$, which lies seven orders of magnitude below the signal $\Delta_\mathbb{T} \sim 5 \times 10^{-2}$ and far below the marker size in Figs. 2 and 3. The uncertainty on all displayed asymmetry values is therefore bounded by this estimate.

Appendix C: Scaling Analysis: Role of Observation Distance and System Size

The directional asymmetry $\Delta_\mathbb{T}$ depends on the observation distance d and the skin length ξ. Since our QLIF is computed from the normalized density matrix [Eq. (7) in the main text], the absolute eigenstate weight r^{j_0} at the initial position j_0 cancels between numerator and denominator. The physically relevant quantity is the *ratio* of eigenstate amplitudes at the two observation sites:

$$\frac{|\psi(j_0 + d)|}{|\psi(j_0 - d)|} = r^{2d} = e^{-2d/\xi}, \tag{C1}$$

which is independent of j_0. This justifies the use of d/ξ as the controlling scale for the directional asymmetry.

To verify this, we perform two numerical experiments.

1. System-Size Independence

We compute $\Delta_\mathbb{T}(\gamma)$ at fixed observation distance $d = 6$ for four system sizes $L = 20, 42, 60, 80$ (corresponding to $j_0 = 10, 20, 30, 40$). As shown in Fig. 3, the curves converge rapidly with increasing L. In particular:

- The suppression at large $|\gamma|$ is insensitive to L, confirming that it is not governed by j_0/ξ.
- The residual L-dependence at moderate $|\gamma|$ reflects finite-size effects (boundary reflections in short chains), which diminish as L increases.

2. Observation-Distance Dependence

We compute $\Delta_\mathbb{T}(\gamma)$ at fixed $L = 42$ for four observation distances $d = 3, 6, 9, 12$. As shown in Fig. 4, d has a dramatic effect:

- The peak amplitude at $d = 3$ is roughly four times that at $d = 6$, while $d = 12$ yields a nearly vanishing signal.
- The peak position in $|\gamma|$ shifts with d: smaller d allows the asymmetry to persist to larger $|\gamma|$ values, consistent with the d/ξ scaling.

Comparing Figs. 3 and 4, the d-dependence is far stronger than the L-dependence, confirming that d/ξ—not j_0/ξ—is the relevant scale for the directional asymmetry measured by QLIF.

3. Robustness of Three Temporal Regimes

To demonstrate that the three temporal regimes identified in the main text persist in the thermodynamic limit, we compute the full QLIF time evolution for system sizes $L = 20, 42, 60, 80$ at fixed $\gamma = 0.3$ and $d = 6$. Figure 5 shows that all three regimes—onset (I), stabilization (II), and oscillation (III)—are clearly visible for every L.

Table IV lists the quantitative regime boundaries extracted from these data. The onset time ($t_I^* = 3.90$), the first oscillation time ($t_{II}^* = 6.55$), and the oscillation period ($T_{\text{osc}} = 2.0$) are all independent of L to within numerical precision. The onset time is determined by the observation distance and the Lieb-Robinson velocity ($t_I^* \approx d/v_{\text{LR}}$), while the oscillation period reflects intrinsic energy-level spacing ($T_{\text{osc}} \sim 2\pi/\Delta E$). Only the oscillation *amplitude* depends on L, decreasing as $L^{-\alpha}$ with $\alpha \approx 0.2$ for $\gamma = 0.3$, because the NHSE concentrates eigenstate weight near boundaries and protects against uniform dilution.

TABLE IV. Regime boundaries for different system sizes at $\gamma = 0.3$, $d = 6$.

L	j_0	t_I^* (onset)	t_{II}^* (1st osc.)	T_{osc}
20	10	3.90	6.55	2.10
42	20	3.90	6.55	2.00
60	30	3.90	6.55	2.00
80	40	3.90	6.55	2.00

4. Robustness of Velocity Ordering

The velocity ordering $v_{\text{eff}}(\gamma < 0) > v_{\text{eff}}(0) > v_{\text{eff}}(\gamma > 0)$ is a key prediction of NHSE blocking. To test its robustness, we measure the onset time t^* versus distance d

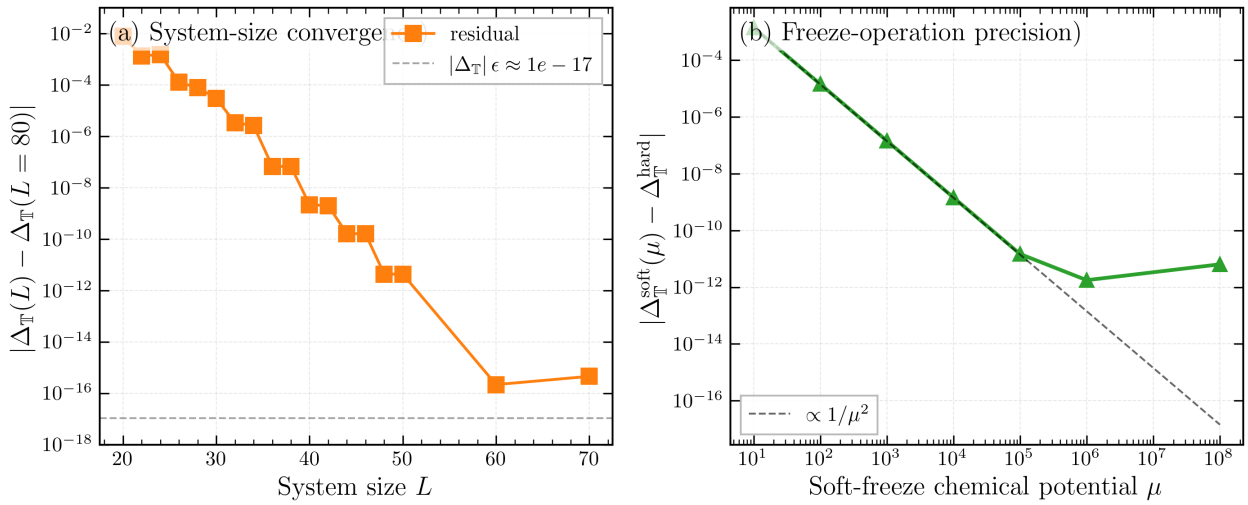

FIG. 2. Numerical convergence of the QLIF asymmetry $\Delta_{\mathbb{T}}(t{=}10)$ at the working point $d = 6$, $\gamma = 0.3$. (a) System-size convergence: $|\Delta_{\mathbb{T}}(L) - \Delta_{\mathbb{T}}(L{=}80)|$ decays exponentially in L; agreement with the $L = 80$ reference is better than 2×10^{-9} at the working size $L = 42$. The grey dashed line marks the floating-point cancellation floor $|\Delta_{\mathbb{T}}|\,\epsilon \approx 10^{-17}$. (b) Freezing-operation precision at $L = 42$: soft freeze converges to hard freeze as $1/\mu^2$, reaching $\sim 10^{-9}$ at $\mu = 10^4$ and saturating near floating-point precision for $\mu \geq 10^6$; the hard-freezing scheme used in the main text is the exact $\mu \to \infty$ limit. The time step dt is omitted because exact matrix exponentiation makes $\Delta_{\mathbb{T}}$ bit-identical across $dt \in [0.005, 0.1]$.

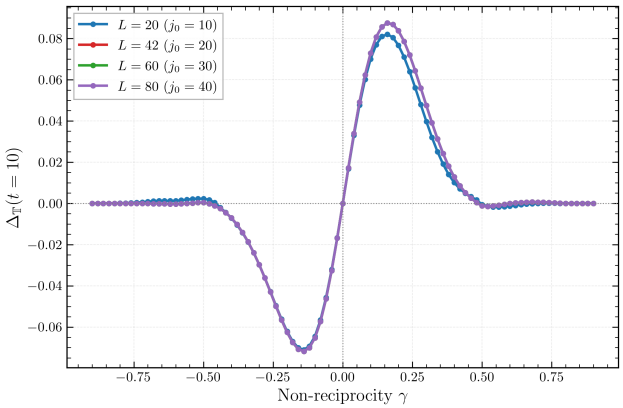

FIG. 3. Directional asymmetry $\Delta_{\mathbb{T}}(t = 10)$ versus γ at fixed observation distance $d = 6$ for system sizes $L = 20, 42, 60, 80$. The curves converge with increasing L, demonstrating that $j_0 = L/2$ is not the controlling scale. Initial state: $|\psi_0\rangle = |j_0, \alpha\rangle$ at the central unit cell; $\alpha\alpha\alpha$ configuration; $t_1 = 1$, $t_2 = 0.5$.

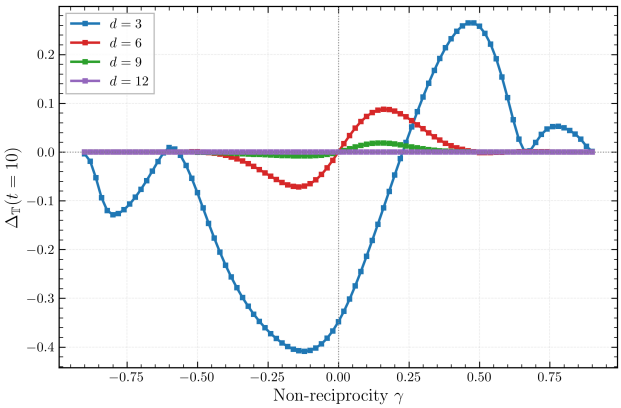

FIG. 4. Directional asymmetry $\Delta_{\mathbb{T}}(t = 10)$ versus γ at fixed $L = 42$ for observation distances $d = 3, 6, 9, 12$. The observation distance d has a dramatic effect on both the amplitude and peak position, in sharp contrast to the weak L-dependence in Fig. 3. Initial state: $|\psi_0\rangle = |j_0, \alpha\rangle$ at the central unit cell ($j_0 = 20$). Parameters: $t_1 = 1$, $t_2 = 0.5$. Note: $d = 6, 12$ yield $\alpha\alpha\alpha$ configurations (all sites on α sublattice), while $d = 3, 9$ yield $\alpha\beta\beta$ configurations (observation sites on β sublattice), which introduces a structural offset at $\gamma = 0$ as discussed in the main text (Fig. 4).

for three system sizes $L = 42, 60, 80$ at $\gamma = -0.3, 0, +0.3$. Figure 6 shows that the $t^*(d)$ curves are identical across all L values, with effective velocities:

$$v_{\mathrm{eff}}(-0.3) = 3.19, \quad v_{\mathrm{eff}}(0) = 2.72, \quad v_{\mathrm{eff}}(+0.3) = 2.13, \tag{C2}$$

independent of system size. This confirms that the velocity ordering is a bulk property determined by the local hopping structure, not a finite-size artifact.

Appendix D: Robustness across the Topological Phase Boundary

To assess whether the main conclusions of this work depend on the topological character of the underlying Hermitian band structure, we repeat the scissors-effect analysis in the trivial phase by raising t_2 from 0.5 to 1.5, keeping all other parameters as in the main-text simula-

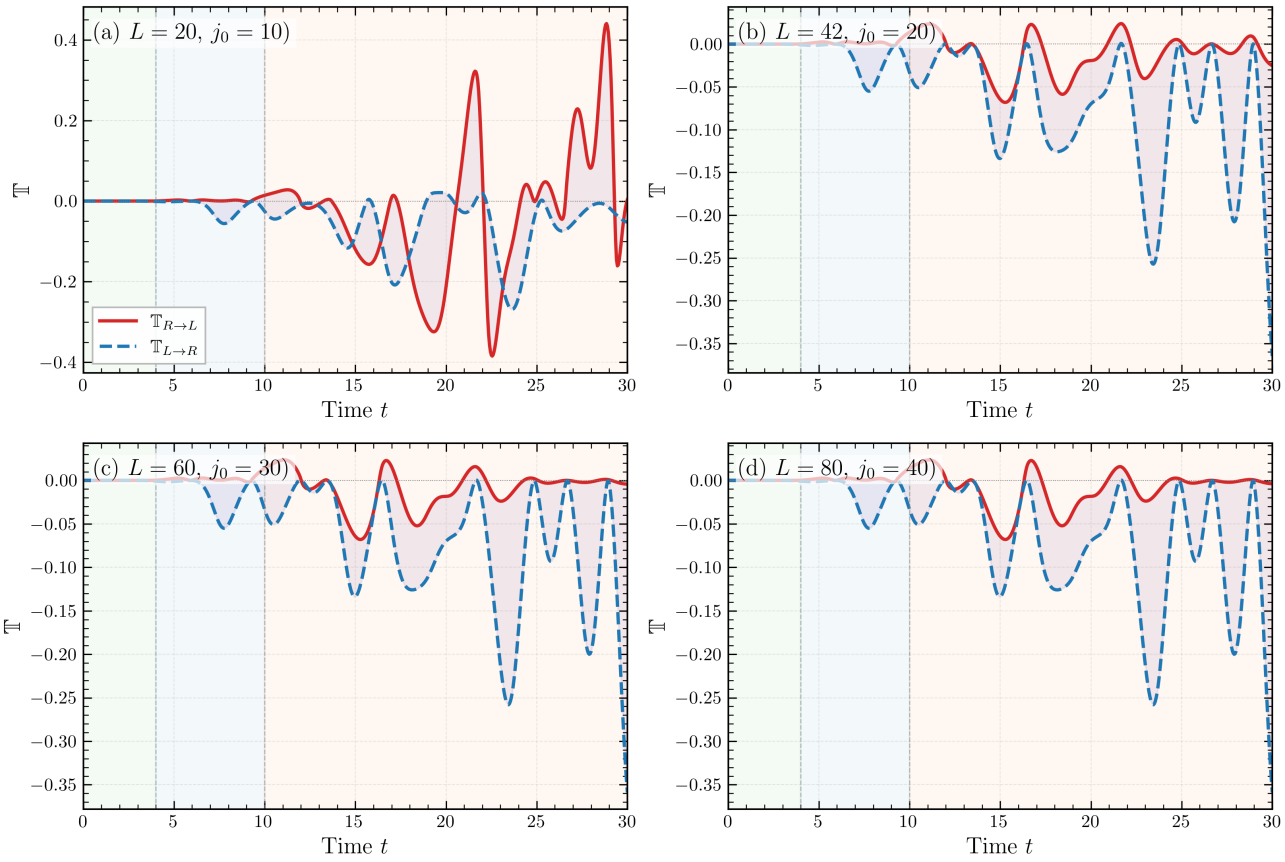

FIG. 5. Time evolution of $\mathbb{T}_{R\to L}$ (solid red) and $\mathbb{T}_{L\to R}$ (dashed blue) for (a) $L = 20$, (b) $L = 42$, (c) $L = 60$, (d) $L = 80$, at fixed $\gamma = +0.3$ and $d = 6$. Shaded regions mark regimes I (onset), II (stabilization), and III (oscillation). The three-regime structure is robust across all system sizes; only the oscillation amplitude decreases with L. Initial state: $|\psi_0\rangle = |j_0, \alpha\rangle$ at the central unit cell; $\alpha\alpha\alpha$ configuration; $t_1 = 1$, $t_2 = 0.5$.

tions ($L = 42$, $t_1 = 1$, $d = 6$, $T_{\max} = 20$).

Figure 7 compares the two phases. Panels (a)–(c) show the time evolution of the cumulative QLIF at three representative values of the non-reciprocity parameter; panel (d) shows $\Delta_{\mathbb{T}}(\gamma)$ at $t = 10$. Three features established in the topological phase remain valid in the trivial phase: (i) the Hermitian limit $\gamma = 0$ enforces a vanishing directional asymmetry; (ii) the sign rule $\mathrm{sgn}(\Delta_{\mathbb{T}}) = \mathrm{sgn}(\gamma)$ holds throughout the scanned range; and (iii) the slope of $\Delta_{\mathbb{T}}(\gamma)$ near $\gamma = 0$ is essentially unchanged across the phase boundary.

The only notable phase-dependent feature is a vertical offset of the cumulative QLIF at $\gamma = 0$, which we attribute to the change in the group-velocity scale $v_{\max} = \min(t_1, t_2)$ that controls how rapidly the initially localized state spreads beyond the observation window. This offset affects the overall magnitude but not the γ-induced directional asymmetry that constitutes the central phenomenon of this paper.

We emphasize that this parallel verification does not resolve the behavior of QLIF *at* the topological transition point $t_2 = t_1$, where the gap closes and the generalized Brillouin zone becomes non-analytic. A systematic investigation of the interplay between non-Hermitian topology and the skin effect on directional information flow is left to future work, as discussed in Section V.

Appendix E: QLIF on the Hatano–Nelson Chain: Model Independence of the Directional Signatures

To test whether the directional QLIF phenomena reported in the main text are specific to the SSH sublattice structure or are intrinsic to the non-Hermitian skin effect itself, we repeat the central analysis on the Hatano–Nelson (HN) chain [12], the simplest one-dimensional non-reciprocal model. The HN chain has a single band, no sublattice, and no line-gap topology; any feature that survives on this model is therefore a property of non-reciprocity per se, not of SSH topology.

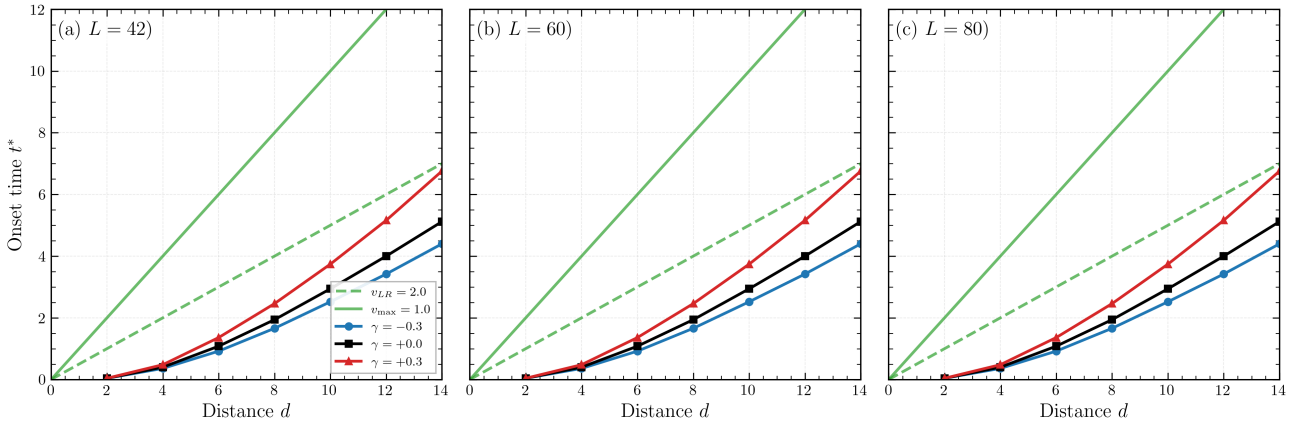

FIG. 6. Onset time t^* (threshold $\epsilon = 10^{-6}$) versus distance d for (a) $L = 42$, (b) $L = 60$, (c) $L = 80$, at $\gamma = -0.3$ (blue circles), 0 (black squares), $+0.3$ (red triangles). Solid green: $v_{\max} = 1.0$; dashed green: $v_{\mathrm{LR}} = 2.0$. The velocity ordering is identical across all system sizes, confirming its robustness in the thermodynamic limit. Initial state: $|\psi_0\rangle = |j_0, \beta\rangle$ at the central unit cell; $t_1 = 1$, $t_2 = 0.5$.

1. Model and protocol

The Hatano–Nelson Hamiltonian, in single-particle form with open boundary conditions, reads

$$H = \sum_{j=1}^{L-1} \left[(t+\gamma)\, c_{j+1}^\dagger c_j + (t-\gamma)\, c_j^\dagger c_{j+1} \right], \qquad \text{(E1)}$$

with $t = 1$ and non-reciprocity parameter γ. We use $L = 43$ sites (odd, so that the central site is unambiguous) and initialize $|\psi_0\rangle = c_{j_0}^\dagger |0\rangle$ at $j_0 = 21$. Observation sites are placed symmetrically at $j_0 \pm d$ with $d = 6$. The cumulative QLIF and the freezing prescription follow Sec. II of the main text and Appendix B without modification.

The imaginary-gauge argument used in Sec. IV of the main text applies verbatim: the similarity transformation $S = \mathrm{diag}(r^{-j})$ with $r = \sqrt{(t-\gamma)/(t+\gamma)}$ maps Eq. (E1) to a Hermitian reference Hamiltonian. The ratio of eigenstate amplitudes at the two observation sites is again $r^{\pm 2d}$, so the same mechanism that drives the SSH scissors effect should drive the HN scissors effect.

2. Numerical results

Figure 8 shows the cumulative QLIF on the HN chain for $\gamma = 0, +0.3, -0.3$ together with the asymmetry scan $\Delta_{\mathbb{T}}(\gamma)$. Three features mirror the SSH results of Sec. III:

1. **Hermitian-limit symmetry.** At $\gamma = 0$ the two directional QLIFs agree to machine precision across the entire evolution window: $\max_t |\mathbb{T}_{R\to L}(t) - \mathbb{T}_{L\to R}(t)|_{\gamma=0} \lesssim 10^{-15}$.

2. **Sign rule and mirror antisymmetry.** For $\gamma = \pm 0.3$ the asymmetry satisfies $\Delta_{\mathbb{T}}(+0.3) = -\Delta_{\mathbb{T}}(-0.3)$ to all displayed digits; the sign of $\Delta_{\mathbb{T}}$ is opposite to the skin-localization direction, reproducing the rule $\mathrm{sgn}(\Delta_{\mathbb{T}}) = -\mathrm{sgn}(\text{skin direction})$ established in the SSH analysis.

3. **Optimal regime.** $\Delta_{\mathbb{T}}(\gamma)$ is non-monotonic, with peaks near $|\gamma| \approx 0.20$. The slope at the origin, $d\Delta_{\mathbb{T}}/d\gamma \approx -0.11$, has magnitude comparable to (within $\sim 20\%$ of) the SSH value of Fig. 1; the opposite sign is a convention artifact, with $\gamma > 0$ favoring $+x$ in the HN convention and $-x$ in the SSH/Yao–Wang convention.

The reproduction of all three features—on a model without any of the SSH structural ingredients—confirms that the directional QLIF signatures originate in non-reciprocity itself. SSH topology only modulates quantitative details (notably through the t_2-dependent effective skin length), not the existence of the phenomena.

[1] W. P. Su, J. R. Schrieffer, and A. J. Heeger, Solitons in polyacetylene, Phys. Rev. Lett. **42**, 1698 (1979).
[2] R. Ghosh, B. Yi, and S. Bose, Quantum Liang information flow probe of causality across critical points, Phys. Rev. Lett. **134**, 150202 (2025).
[3] S. Yao and Z. Wang, Edge states and topological invariants of non-Hermitian systems, Phys. Rev. Lett. **121**, 086803 (2018).
[4] E. H. Lieb and D. W. Robinson, The finite group velocity of quantum spin systems, Commun. Math. Phys. **28**, 251

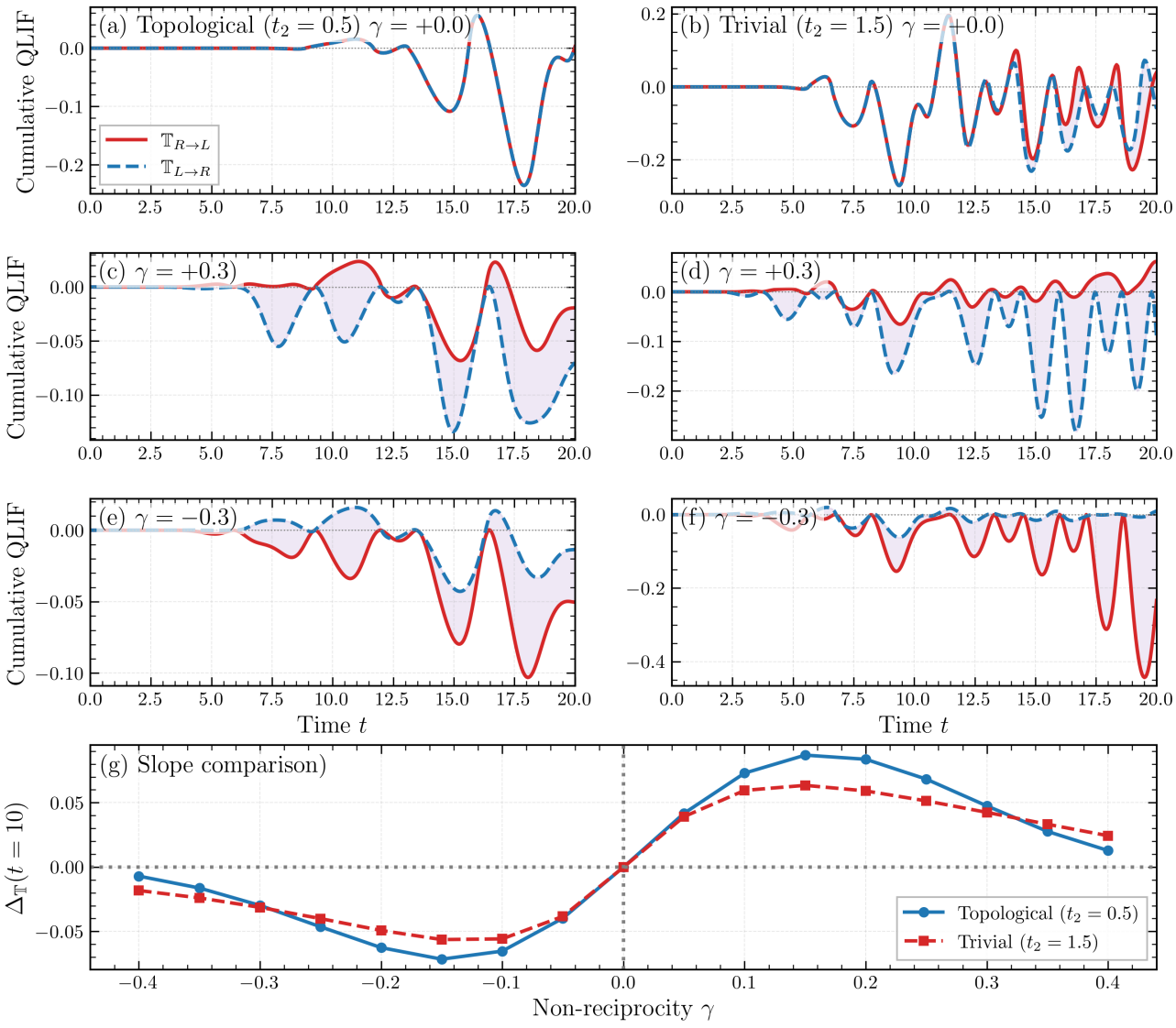

FIG. 7. Robustness of the scissors effect across the topological phase boundary. Left column: topological phase ($t_2 = 0.5$). Right column: trivial phase ($t_2 = 1.5$). Rows (a)–(c): cumulative QLIF $\mathbb{T}_{R\to L}$ (solid) and $\mathbb{T}_{L\to R}$ (dashed) at $\gamma = 0, +0.3, -0.3$; the shaded band indicates the directional asymmetry $\Delta_{\mathbb{T}}$. Row (d): $\Delta_{\mathbb{T}}(t = 10)$ versus γ for both phases; the linear slopes near $\gamma = 0$ are $+0.14$ (topological) and $+0.13$ (trivial). Other parameters as in Fig. 2.

(1972).
[5] S. Bravyi, M. B. Hastings, and F. Verstraete, Lieb-Robinson bounds and the generation of correlations and topological quantum order, Phys. Rev. Lett. **97**, 050401 (2006).
[6] B. Dóra and C. P. Moca, Quantum quench in PT-symmetric Luttinger liquid, Phys. Rev. Lett. **124**, 136802 (2020).
[7] X. Turkeshi and M. Schirò, Entanglement and correlation spreading in non-Hermitian spin chains, Phys. Rev. B **107**, L020403 (2023).
[8] B. Barch, Locality, correlations, information, and non-Hermitian quantum systems, Phys. Rev. B **110**, 094307 (2024).
[9] F. Evers and A. D. Mirlin, Anderson transitions, Rev. Mod. Phys. **80**, 1355 (2008).
[10] L.-J. Zhai, L.-L. Hou, Q. Gao, and H.-Y. Wang, Kibble–Zurek scaling of the dynamical localization–skin effect phase transition in a non-Hermitian quasi-periodic system under the open boundary condition, Front. Phys. **10**, 1098551 (2022).
[11] J.-L. Liu, T.-F. Pang, X.-S. Yang, and Z.-L. Wang, Skin effect in disordered non-Hermitian Su-Schrieffer-Heeger, Acta Phys. Sin. **71**, 227402 (2022).
[12] N. Hatano and D. R. Nelson, Localization transitions in non-Hermitian quantum mechanics, Phys. Rev. Lett. **77**, 570 (1996).

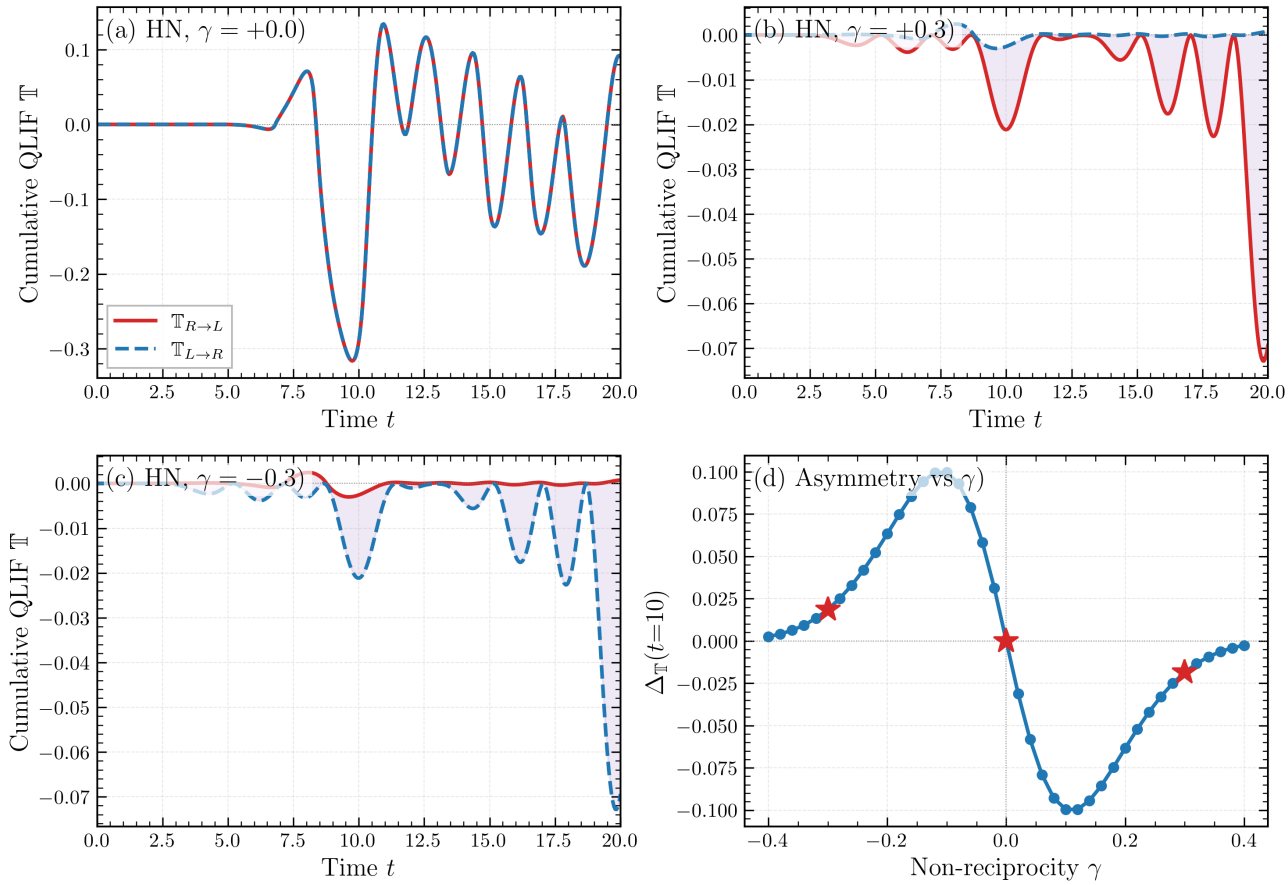

FIG. 8. Directional QLIF on the Hatano–Nelson chain ($L = 43$, $j_0 = 21$, $d = 6$, $t = 1$). (a)–(c) Cumulative $\mathbb{T}_{R\to L}$ and $\mathbb{T}_{L\to R}$ versus time for $\gamma = 0, +0.3, -0.3$. The Hermitian case (a) shows exact symmetry; the non-reciprocal cases (b),(c) are perfect mirror images of each other. (d) Asymmetry $\Delta_{\mathbb{T}}(t = 10)$ versus γ; red stars mark the three main-panel values. The scissors effect, sign rule, and non-monotonic optimal-regime peak all reproduce the SSH results of Fig. 1, despite the absence of any sublattice or topological structure.